



Saturn's seasonal variability from four decades of ground-based mid-infrared observations

James S.D. Blake, L.N. Fletcher, G.S. Orton, A. Antuñano, M.T. Roman, Y. Kasaba, T. Fujiyoshi, H. Melin, D. Bardet, J.A. Sinclair, et al.

► To cite this version:

James S.D. Blake, L.N. Fletcher, G.S. Orton, A. Antuñano, M.T. Roman, et al.. Saturn's seasonal variability from four decades of ground-based mid-infrared observations. *Icarus*, 2023, 392, pp.115347. <10.1016/j.icarus.2022.115347>. <hal-03950031>

HAL Id: hal-03950031

<https://hal.science/hal-03950031v1>

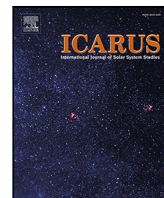
Submitted on 26 Jan 2023

HAL is a multi-disciplinary open access archive for the deposit and dissemination of scientific research documents, whether they are published or not. The documents may come from teaching and research institutions in France or abroad, or from public or private research centers.

L'archive ouverte pluridisciplinaire **HAL**, est destinée au dépôt et à la diffusion de documents scientifiques de niveau recherche, publiés ou non, émanant des établissements d'enseignement et de recherche français ou étrangers, des laboratoires publics ou privés.



Distributed under a Creative Commons CC BY 4.0 - Attribution - International License



Research Paper

Saturn's seasonal variability from four decades of ground-based mid-infrared observations

James S.D. Blake^a, L.N. Fletcher^{a,*}, G.S. Orton^b, A. Antuñano^c, M.T. Roman^a, Y. Kasaba^d,
T. Fujiyoshi^e, H. Melin^a, D. Bardet^a, J.A. Sinclair^b, M. Es-Sayeh^f

^a School of Physics & Astronomy, University of Leicester, University Road, Leicester, LE1 7RH, UK

^b Jet Propulsion Laboratory, California Institute of Technology, 4800 Oak Grove Drive, Pasadena, CA, 91109, USA

^c UPV/EHU, Escuela Ingeniería de Bilbao, Física Aplicada, Spain

^d Planetary Plasma and Atmospheric Research Center, Graduate School of Science, Tohoku University, Sendai, Miyagi, 980-8578, Japan

^e Subaru Telescope, National Astronomical Observatory of Japan, 650 North A'ohoku Pl., Hilo, HI 96720, USA

^f Institut de Physique du Globe de Paris, Université de Paris, 35 rue Hélène Brion, 75013, Paris, France

ARTICLE INFO

Keywords:

Saturn
Composition
Atmospheres
Dynamics

ABSTRACT

A multi-decade record of ground-based mid-infrared (7–25 μm) images of Saturn is used to explore seasonal and non-seasonal variability in thermal emission over more than a Saturnian year (1984–2022). Thermal emission measured by 3-m and 8-m-class observatories (notably NASA's Infrared Telescope Facility, Subaru, and ESO's Very Large Telescope) compares favourably with synthetic images based on both Cassini-derived temperature records and the predictions of radiative climate models. We find that 8-m class facilities are capable of resolving thermal contrasts on the scale of Saturn's belts, zones, polar hexagon, and polar cyclones, superimposed onto large-scale seasonal asymmetries. Seasonal changes in brightness temperatures of ~ 30 K in the stratosphere and ~ 10 K in the upper troposphere are observed, as the northern and southern polar stratospheric vortices (NPSV and SPSV) form in spring and dissipate in autumn. The timings of the first appearance of the warm polar vortices is successfully reproduced by radiative climate models, confirming them to be radiative phenomena, albeit entrained within sharp boundaries influenced by dynamics. Axisymmetric thermal bands (4–5 per hemisphere) display temperature gradients that are strongly correlated with Saturn's zonal winds, indicating winds that decay in strength with altitude from the cloud-tops to the ~ 1 -mbar level, and implying meridional circulation cells in Saturn's upper troposphere and stratosphere forming the system of cool zones and warm belts. Saturn's thermal structure is largely repeatable from year to year (via comparison of infrared images in 1989 and 2018), with the exception of low-latitudes. Here we find evidence of inter-annual variations because the equatorial banding at $7.9 \mu\text{m}$ is inconsistent with a ~ 15 -year period for Saturn's equatorial stratospheric oscillation, i.e., it is not strictly semi-annual. Either the oscillation has a longer period closer to ~ 20 years, or its progression is naturally variable and interrupted by tropospheric meteorology (e.g., storms). Finally, observations between 2017–2022 extend the legacy of the Cassini mission, revealing the continued warming of the NPSV during northern summer in line with predictions of radiative climate models.

1. Introduction

Saturn's axial tilt of 26.7° subjects its atmosphere to seasonal cycles of temperatures, aerosols, and chemistry during its 29.5-year orbit of the Sun. Superimposed onto the seasonal hemispheric asymmetries in temperature and composition are smaller-scale phenomena associated with dynamics, such as belt/zone contrasts (Fletcher et al., 2007), the formation of polar vortices (Orton and Yanamandra-Fisher, 2005; Fletcher et al., 2018b), equatorial stratospheric oscillations (Fouchet

et al., 2008; Orton et al., 2008), inter-hemispheric circulation patterns (Guerlet et al., 2009; Friedson and Moses, 2012; Bardet et al., 2022), and perturbations from giant storms (Fletcher et al., 2012). The Cassini spacecraft, which orbited Saturn from July 2004 (planetocentric solar longitude $L_s = 293^\circ$, northern winter) to September 2017 ($L_s = 93^\circ$, northern summer), provided an unprecedented record of seasonal variability over almost half a Saturn year from solstice to solstice, and almost from perihelion ($L_s = 280^\circ$, June 2003) to aphelion ($L_s = 100^\circ$, April 2018), as reviewed by Fletcher et al. (2018a).

* Corresponding author.

E-mail address: leigh.fletcher@leicester.ac.uk (L.N. Fletcher).

<https://doi.org/10.1016/j.icarus.2022.115347>

Received 2 August 2022; Received in revised form 12 October 2022; Accepted 7 November 2022

Available online 21 November 2022

0019-1035/© 2022 The Authors. Published by Elsevier Inc. This is an open access article under the CC BY license (<http://creativecommons.org/licenses/by/4.0/>).

However, to understand Saturn's atmosphere over longer periods of time, we rely on the extensive time series provided by ground-based observatories before, during, and after the Cassini epoch. Over the past four decades, Saturn's thermal emission has been observed from numerous facilities, most notably NASA's Infrared Telescope Facility (IRTF), ESO's Very Large Telescope (VLT), and the Subaru Observatory (the former since 1984, the latter two starting in 2005, Fletcher et al., 2009b). Observations during the Cassini mission provided mission support, whereas IRTF observations allow us fill the gap between the Voyager-1 (1980, $L_s = 8.6^\circ$) and Voyager-2 (1981, $L_s = 18.2^\circ$) encounters (Hanel et al., 1981, 1982) and Cassini's arrival (2004, $L_s = 293^\circ$).

Mid-IR imaging observations have been previously published to provide snapshots of Saturn at certain times: for example, central-meridian scans at $11.7\ \mu\text{m}$ (sensing stratospheric ethane), taken at Palomar in 1973 by Gillett and Orton (1975), first revealed Saturn's bright South Polar Stratospheric Vortex (SPSV) during southern summer, a warm hood extending some $\sim 15^\circ$ latitude from the pole (also observed in 1977–78 in $7.8\text{--}12.7\text{-}\mu\text{m}$ bolometric scans from the Mauna Kea Observatory, Sinton et al., 1980). Gezari et al. (1989) then revealed a similarly warm North Polar Stratospheric Vortex (NPSV) in 1989 using 2D mid-infrared imaging; Orton and Yanamandra-Fisher (2005) discovered a central south polar cyclone (SPC) within the SPSV using Keck in 2004. Orton et al. (2008) used images between 1984 and 2007 to explore Saturn's equatorial stratospheric oscillation and its ~ 15 -year period; Fletcher et al. (2011b) and Fletcher et al. (2012) observed the tropospheric and stratospheric perturbations associated with a giant storm in Saturn's northern hemisphere; and Fletcher et al. (2017) investigated how that same storm disrupted the equatorial oscillation. However, to date there have been few systematic studies of ground-based imaging data over multiple decades to explore interconnected phenomena that evolve in a cyclic fashion. In particular, the ground-based data presented in this study constrain the seasonal onset, growth, and dissipation of the NPSV and SPSV over more than one Saturn year (Gezari et al., 1989; Orton and Yanamandra-Fisher, 2005; Fletcher et al., 2018b); as well as the modulation of equatorial stratospheric brightness by Saturn's equatorial stratospheric oscillation (Orton et al., 2008; Fletcher et al., 2017).

Collectively, these phenomena lead to a complex seasonal progression for Saturn's atmosphere. This study uses the 1984–2022 archive of mid-IR imaging (Section 2) to present a long term seasonal analysis of Saturn's atmosphere, focusing on three themes. Section 3 uses the Cassini record of Saturn's temperatures between 2004–2017 to reproduce the observed emission in ground-based images during southern summer and northern spring. We demonstrate how observations from 8-m class observatories can be used to retrieve Saturn's thermal structure and the windshear associated with its belts and zones. Section 4 then assesses whether the same temperatures, alongside radiative–convective models, can reproduce images from the IRTF in the 1980s (Gezari et al., 1989) to determine the extent of inter-annual variability in Saturn's seasonal response. Finally, Section 5 considers how Saturn has changed since the demise of Cassini, using VLT and Subaru data beyond 2017.

2. Observations

Saturn's mid-IR spectrum is shaped by the collision-induced opacity of hydrogen and helium, absorption bands of tropospheric PH_3 and NH_3 , and emission bands of CH_4 and photochemically-produced hydrocarbons (primarily C_2H_2 and C_2H_6). A standard set of imaging filters, as shown in Figure 1 of Fletcher et al. (2009b), would include Q-band filters sounding 80–350 mbar tropospheric temperatures from the H_2 –He continuum between 17 and $25\ \mu\text{m}$, and N-band filters sounding 0.5–5 mbar stratospheric temperatures via CH_4 emission at $7.9\ \mu\text{m}$ and C_2H_6 emission at $12.3\ \mu\text{m}$. Additional N-band filters were sometimes

included, sounding tropospheric PH_3 (400–800 mbar) between $8\text{--}11\ \mu\text{m}$, and stratospheric C_2H_2 (0.5–15 mbar) at $13.7\ \mu\text{m}$.

Reduction of mid-IR imaging follows the scheme outlined by Fletcher et al. (2009b). Saturn is detected differentially on top of the IR-bright sky background via the chopping and nodding technique, subtracting contributions from the sky and telescope. Image navigation and geometrical registration requires fitting a planetary silhouette over the image to determine latitudes, longitudes, and emission angles, before producing an equirectangular map of the data. Given the low reliability of absolute calibration via stellar comparison on non-photometric nights, data were calibrated by scaling the observed flux at low latitudes (and excluding ring absorption) to a low-latitude average of Cassini/CIRS data, as described by Fletcher et al. (2009b) and further detailed below. Whilst such a calibration is crude, it enables the creation of a consistent dataset for studying relative brightness changes, but would not capture absolute changes in Saturn's global temperatures over time.

2.1. VLT/VISIR 2008–2022

Saturn was regularly observed by the Very Large Telescope (VLT) Imager and Spectrometer for the mid-infrared (VISIR, Lagage et al., 2004) between 2008 and 2022. VISIR was mounted on the 8.2-m UT3 telescope at Paranal for much of this period, albeit with a 3-year period of refurbishment between 2012 and 2015. Prior to the upgrade, the DRS 256×256 BIB detector offered a field of view of $32''$ with a pixel scale of $0.127''/\text{pixel}$, producing the selection of images shown in Fig. 1. We include a single February-2004 mosaicked observation from the Keck Long Wave Spectrometer (LWS) as a comparison immediately prior to Cassini's arrival at Saturn (Orton and Yanamandra-Fisher, 2005). Three wavelengths are shown: 7.8 , 12.2 and $17.6\ \mu\text{m}$, sounding stratospheric methane, ethane, and tropospheric H_2 , respectively, although additional images at 10.3 , 18.7 , and $19.5\ \mu\text{m}$ were also acquired within a single hour-long observing block. The diffraction-limited angular resolution ranges from $0.25''$ at $7.9\ \mu\text{m}$ to $0.6''$ at $19.5\ \mu\text{m}$, which equates to $800\text{--}1900\ \text{km}$ for Saturn near opposition, or $0.75\text{--}1.8^\circ$ latitude at Saturn's equator.

The spatial sampling of VISIR was substantially improved after 2015, using a new 1024×1024 Raytheon Aquarius IBC detector with a pixel scale of $0.045''/\text{pixel}$ over a $38''$ field of view. Although Saturn's rings are often 'clipped' by this field of view, the excellent plate scale offers the high-quality imaging shown in Fig. 2. Indeed, Saturn's thermal hexagon can be seen in both the troposphere- and stratosphere-sensing filters (particularly between 2016 and 2018, when the north pole was in view), confirming that the sinusoidal variation at the edge of the north-polar vortex extends throughout the troposphere and stratosphere (Fletcher et al., 2018b).

Since the upgrade of the VISIR detector in 2015, high-brightness images have suffered from a pattern of vertical and horizontal stripes that must be removed before use. Two techniques were explored: a Gaussian-smooth of the image to identify and subtract high-frequency stripes, and a Fourier transform of the image to identify periodic structures to mask out, before reconstructing the image in the spatial domain. Given the strong variation in flux across the VISIR images associated with Saturn's limb and rings, the latter technique was found to be superior, and was used to develop the image montage in Fig. 2. A full list of observation dates and program numbers are provided in Table A.1, and raw data are available through the ESO archive.¹

¹ http://archive.eso.org/eso/eso_archive_main.html

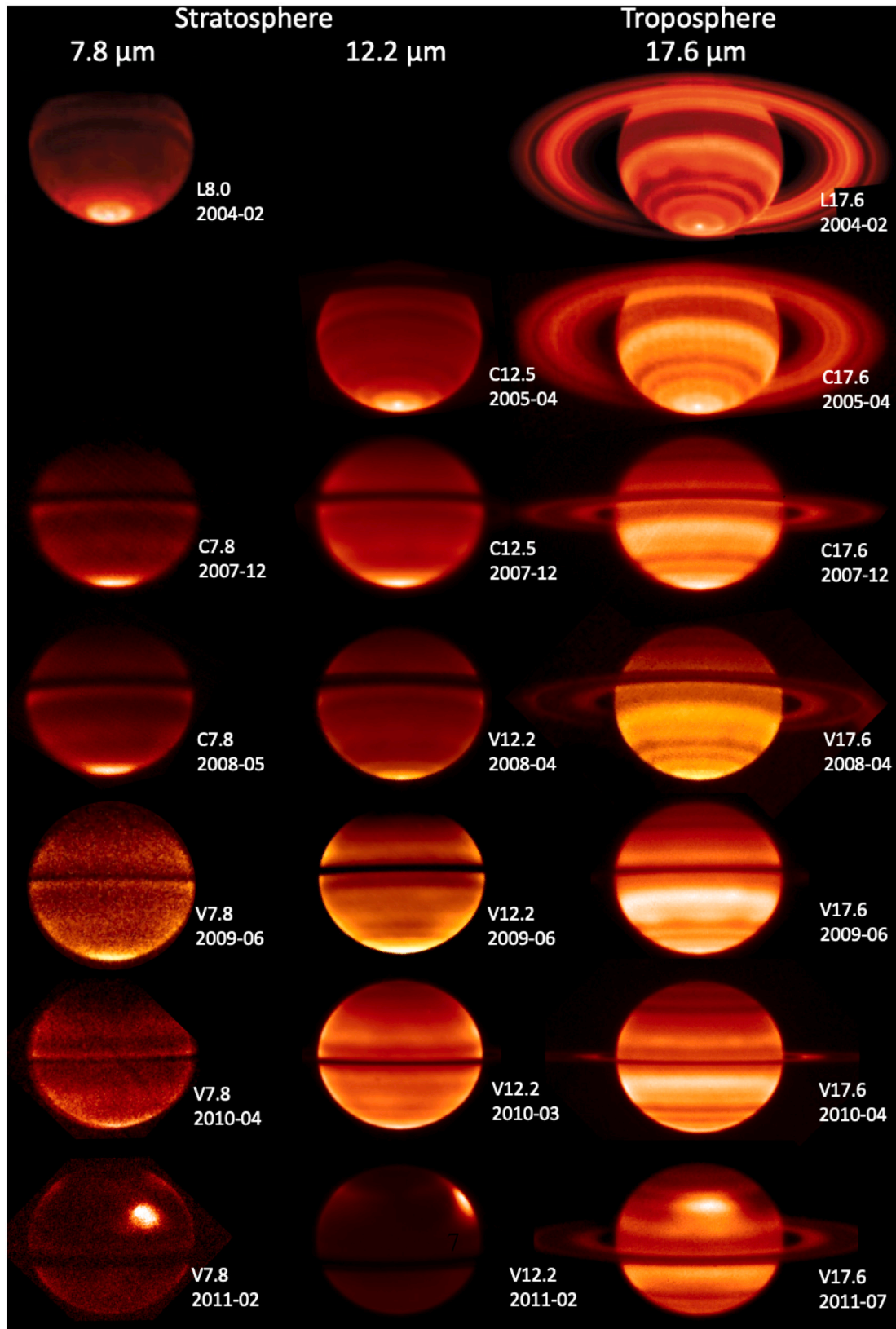


Fig. 1. Observations of Saturn from VLT/VISIR (marked with V), Keck/LWS (marked with an L, [Orton and Yanamandra-Fisher, 2005](#)), and Subaru/COMICS (marked with C) from 2004 to 2011 for the filters 7.8, 12.2 and 17.65 μm . This spans the period before and after the northern spring equinox ($L_s = 0^\circ$) in 2009, and 2011 images appear unusual due to the presence of Saturn's northern storm ([Fletcher et al., 2012](#)).

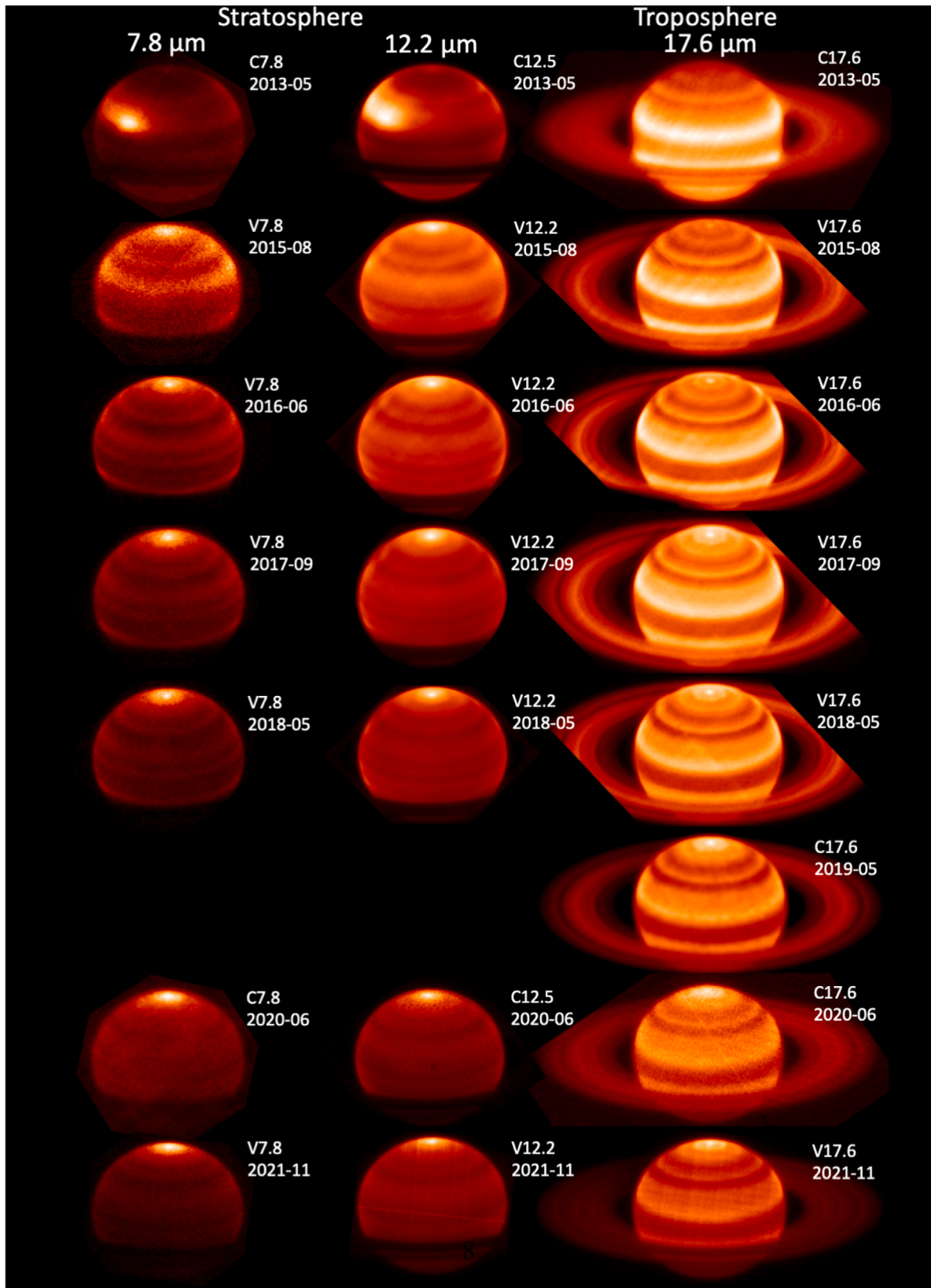


Fig. 2. Observations of Saturn from VLT/VISIR (marked with V) and Subaru/COMICS (marked with C) from 2013–2021, spanning the period surrounding Saturn's northern summer solstice ($L_s = 90^\circ$) for the filters 7.8, 12.2 and 17.65 μm . Note the visibility of Saturn's polar hexagon at 17.6 μm , surrounding the compact warm polar cyclone (PC).

2.2. Subaru/COMICS 2005–2020

VISIR observations were supplemented by images from the Cooled Mid-IR Camera and Spectrograph (COMICS) on the Subaru telescope of Japan (Katata et al., 2002; Okamoto et al., 2003) between 2005 and 2020, a subset of which are shown in Fig. 1 and 2. The COMICS 320×240 array had a coarser plate scale of $0.133''/\text{pixel}$ compared to VISIR, but a larger field of view ($42 \times 32''$), preventing clipping of Saturn's rings. Previously-published observations from April 2005 (Fletcher et al., 2009b) spanned $8.7\text{--}24.5\ \mu\text{m}$, but lacked a $7.8\text{--}\mu\text{m}$ filter sensitive to stratospheric methane. This was added for later datasets in each of the following years: 2007–2009; 2013; and 2017–2020. COMICS was decommissioned in 2020, and raw data are available through the SMOKA archive.² The datasets used in this study are recorded in Table A.1.

2.3. NASA/IRTF 1984–2003

Prior to 2003, mid-IR imaging of Saturn was provided primarily by NASA's Infrared Telescope Facility (IRTF). With its 3-m primary mirror, IRTF provides diffraction-limited imaging with spatial resolutions varying from $0.65\text{--}2.0''$ at $7.9\text{--}24.5\ \mu\text{m}$, equivalent to $2200\text{--}6500\ \text{km}$ for Saturn at opposition, or $2\text{--}6^\circ$ latitude at the equator. Additional blurring arises from atmospheric seeing, which varied from night to night. Between 1984 and 1989, single-element photometers (the BOLO1 and AT1 instruments) were scanned across Saturn to create maps — details of the acquisition and calibration of these data can be found in the supplementary material of Orton et al. (2008).

Observations by Gezari et al. (1989) in March 1989 provided the first two-dimensional infrared observations of Saturn from a ground-based telescope (IRTF). The 1989 images were calibrated using the radiance values listed by Gezari et al. (1989) for the north pole: 2.7 , 9.7 and $20.0\ \text{Jy arcsec}^{-2}$ for filters at $7.8\ \mu\text{m}$, $11.6\ \mu\text{m}$, and $12.4\ \mu\text{m}$, respectively. The raster-scanned data acquired prior to 1989 were calibrated by scaling it to match the 1989 observations of Gezari et al. (1989) where possible, as absolute stellar calibration was not available. The 1984–1990 raster-scanned observations of Orton et al. (2008) and 1989 images of Gezari et al. (1989) are shown in Fig. 3, and the available observations have been added to Table A.1. We note that December 1990 images show interesting low-latitude structures, with brighter emission towards the west that was not apparent in the March 1989 images of Gezari et al. (1989). These data were taken approximately three months after the Great White Storm of September 1990 (Sánchez-Lavega et al., 1991), and may indicate stratospheric perturbations from the storm, as seen in the more recent storm eruption of 2010–2013 (Fletcher et al., 2012).

From the early 1990s, 2D imaging of Saturn with the IRTF instruments became more frequent. MIRAC2 (Mid-Infrared Array Camera, 1993–1997) provided imaging with a $0.34''/\text{pixel}$ scale (at $10\ \mu\text{m}$) and a maximum field-of-view of $44 \times 44''$ (Hoffmann et al., 1993). MIRLIN (1996–2004) was a $128 \times 128\ \text{pixel}$, $7\text{--}25\ \mu\text{m}$ infrared astronomical camera built at JPL and operated on IRTF, with a pixel scale of $0.475''/\text{pixel}$ and a field of view of $61 \times 61''$ (Ressler et al., 1994) for the same filters as MIRAC2. MIRLIN and MIRAC2 images for filters at 7.8 , 12.4 and $18.0\ \mu\text{m}$ have been used in the time series in Fig. 4, approximately covering the period between southern spring equinox ($L_s = 180^\circ$, November 1995) and southern summer solstice ($L_s = 270^\circ$, October 2002), and bringing us to the epoch when Cassini observations and 8-m class facilities were observing regularly. The IRTF images were supplemented in 1995 and 1996 by observations from the SpectroCam-10 instrument on the Hale 200-inch at Palomar (described by Orton et al., 2008).

Two additional sources of IRTF data are not considered as part of this study — imaging from the MIRSI instrument between 2003 and 2012 (Deutsch et al., 2003), and spectral scan maps from the TEXES instrument (Lacy et al., 2002) acquired since 2002 (Greathouse et al., 2005). The former are superseded in this study by the aforementioned VISIR and COMICS observations spanning the same time period with a superior spatial resolution. The spectroscopic maps from TEXES require significantly different processing techniques to ensure a valid comparison to the imaging datasets. These extensive datasets will be the subject of a future study.

3. Comparison of Cassini and ground-based observations 2004–2017

In this Section, we compare observations from 8-m class observatories (VLT and Subaru) to the record of brightness temperatures and retrieved temperatures from the Cassini/CIRS instrument. We explore the ground-based data in the following subsections by (i) generating synthetic images using the CIRS database for comparison to observations of Saturn's seasonal changes (Section 3.1); (ii) measuring brightness temperature gradients to understand Saturn's belt/zone structure (Section 3.2); and (iii) deriving 2D temperature-pressure cross-sections from stacked filtered images (Section 3.3).

Zonal-mean brightness temperatures for COMICS and VISIR observations from 2005–2017 are shown in Fig. 5, compared to filter-integrated brightnesses measured by Cassini. We show a selection of four filters: 7.8 , 10.7 , 17.6 and $18.6\ \mu\text{m}$. These are not true zonal averages, but approximations formed by averaging within $\pm 30^\circ$ longitude of the central meridian for each image, assuming longitudinal homogeneity. This is a good approximation for most dates except for those in 2011–13, where significant longitudinal structure was present due to the northern springtime storm (Fletcher et al., 2012), as observed in Fig. 5(e). Regions obscured by Saturn's rings are omitted for each date, although some high-latitude 'winter-hemisphere' points are included. The ground-based zonal-mean T_B is compared to data from Cassini/CIRS — specifically a database of spectra developed by curtailing CIRS interferograms so that they all have the same length (e.g., 15-cm^{-1} spectral resolution) following Fletcher et al. (2017). The CIRS far-IR focal plane one was used for Q-band observations ($>17\ \mu\text{m}$), whereas the mid-IR focal planes (3 and 4) were used for N-band observations ($7\text{--}13\ \mu\text{m}$). CIRS spectra were convolved with VISIR filter functions to approximate the brightness temperature as seen by the ground-based observatories in Fig. 5(e–h). No attempt has been made to remove limb-brightening/darkening in either dataset.

Fig. 5 shows the seasonal progression of tropospheric and stratospheric temperatures during the course of the Cassini mission. In the stratosphere, the southern-summer T_B ranges from $140\ \text{K}$ at the south pole to $110\ \text{K}$ at the north pole in 2005–2007, but by the end of the Cassini mission in 2017 this gradient had reversed, with peak brightness temperatures of $\sim 140\ \text{K}$ at the north pole. Equatorial stratospheric temperatures at $7.8\ \mu\text{m}$ show variations associated with Saturn's stratospheric oscillation — from a local maximum in equatorial T_B in 2004–06, to a local minimum in equatorial T_B in 2015–17, consistent with the approximately ~ 15 -year period identified by Orton et al. (2008). Although the close-match of the absolute brightness temperatures is unsurprising, given our method of radiometric calibration, the fact that the relative changes in T_B are consistent between Cassini and the ground-based record is encouraging. Seasonal changes in the troposphere are smaller (pole-to-pole contrasts of $\sim 10\text{--}15\ \text{K}$), consistent with the longer radiative timescales of the deeper atmosphere (Conrath et al., 1990). In almost all filters, 2017 (summer solstice) presented the warmest T_B at the north pole, associated with the North Polar Stratospheric Vortex (NPSV) (Fletcher et al., 2018b).

The latitudes of the eastwards peaks in the cloud-tracked zonal winds (García-Melendo et al., 2011) are also shown in Fig. 5. This shows qualitatively that T_B contrasts measured by Cassini and VLT/Subaru are co-located with the peak eastward winds. We assess this quantitatively in Section 3.2.

² <https://smoka.nao.ac.jp/>

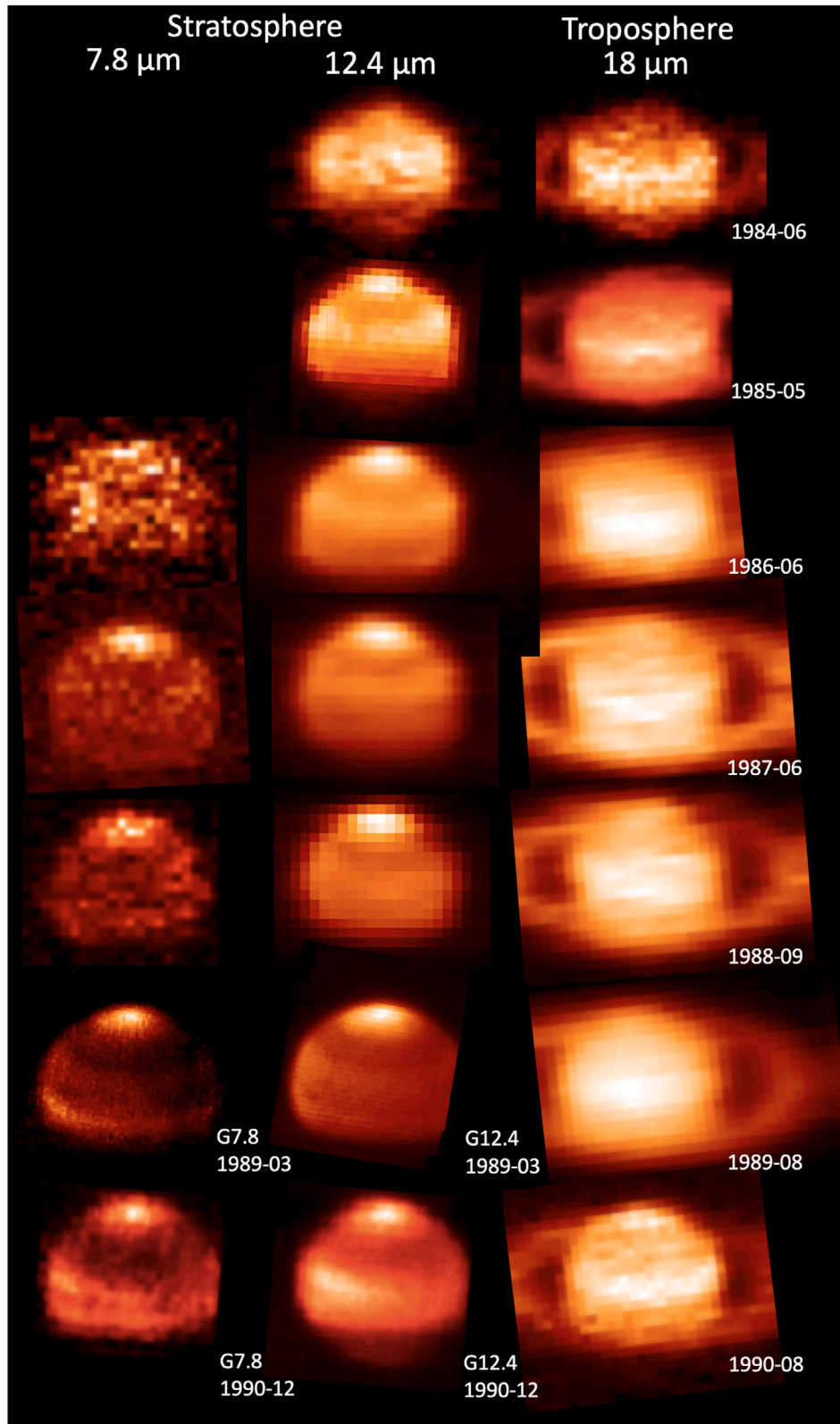


Fig. 3. Observations of Saturn between 1984 and 1990 using the IRTF, spanning the period surrounding northern summer solstice in October 1987 ($L_s = 90^\circ$). Images are primarily from raster-scans using single-element photometers. After 1989, observations used the 2D camera of Gezari et al. (1989), marked with a 'G'. This montage reveals the development of the warm NPSV, and the December-1990 stratospheric images reveal east-west structure that occurred a few months after the September-1990 Great White Storm (Sánchez-Lavega et al., 1991).

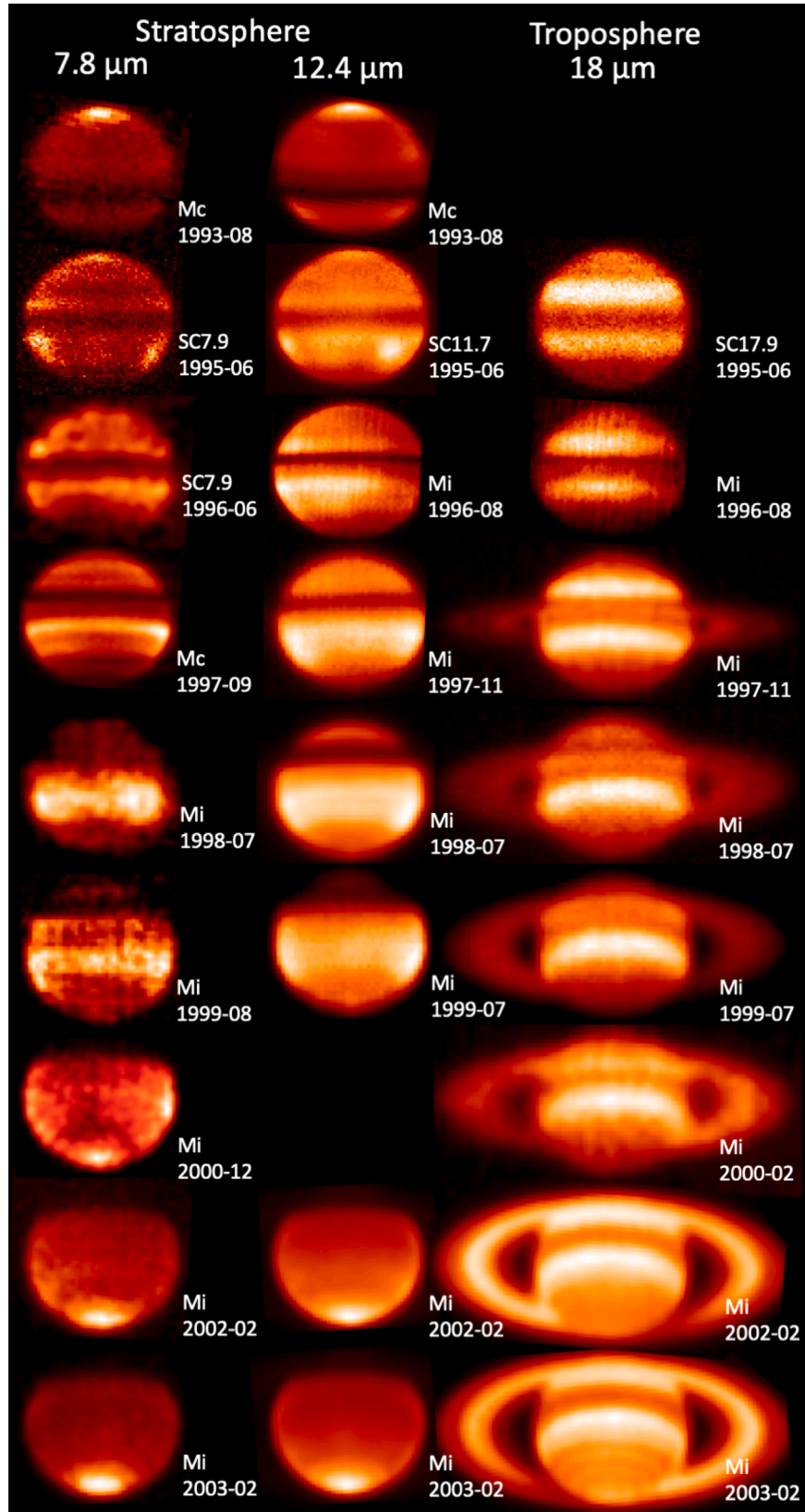


Fig. 4. Observations of Saturn from the MIRLIN (marked Mi) and MIRAC2 (marked with Mc) instruments on the IRTF throughout the 1990s, showing the steady improvement in image quality throughout this period. Observations from SPECTROCAM-10 (mounted on the Hale 200-inch and marked SC, [Orton et al., 2008](#)) are also shown for June 1995 and June 1996, either side of southern spring equinox ($L_s = 180^\circ$).

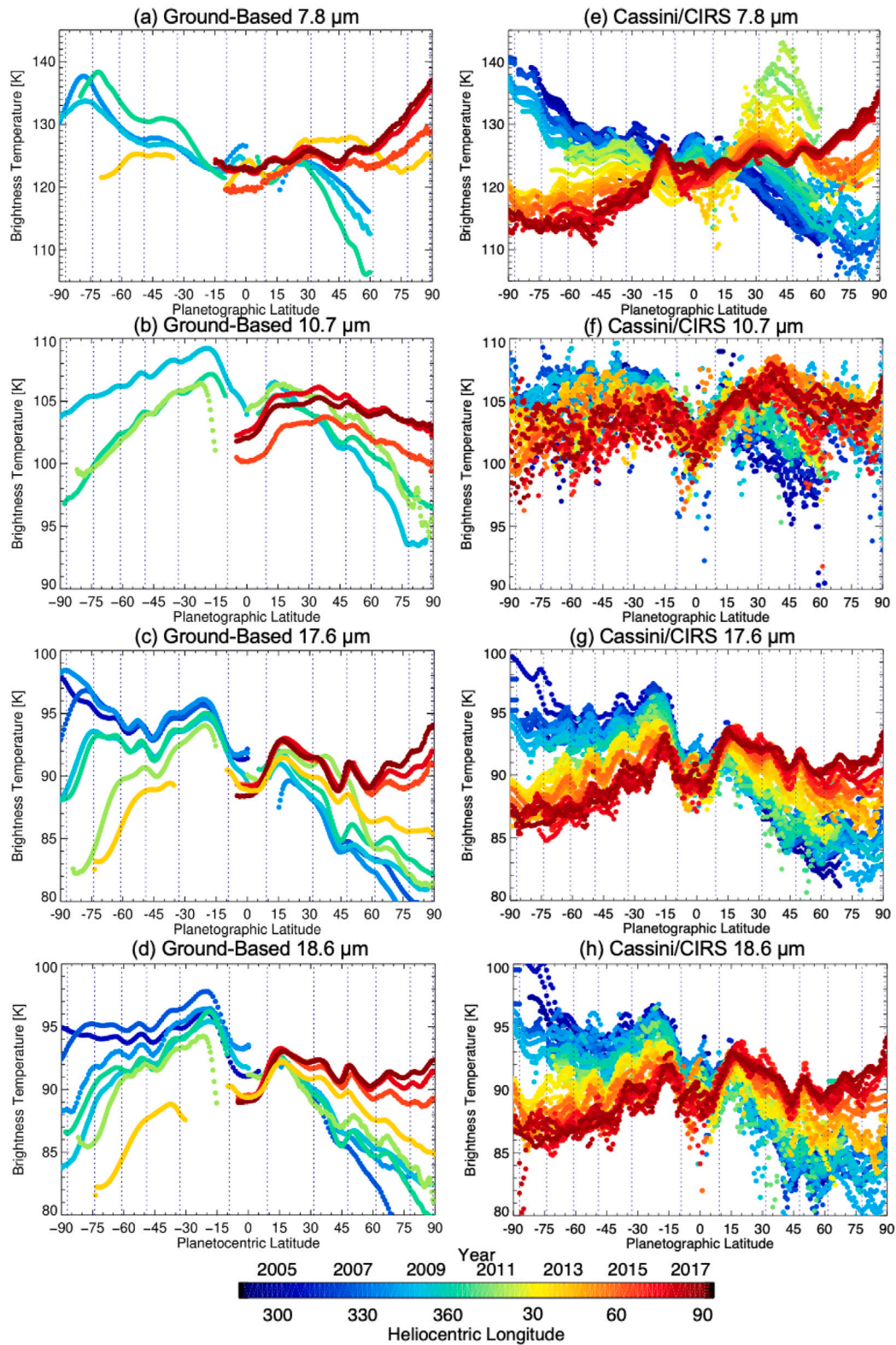


Fig. 5. Seasonal changes in Saturn's brightness temperatures between 2004 and 2017, comparing yearly records from VISIR and COMICS (left) to more regular latitudinal scans from Cassini/CIRS (right). Regions obscured by Saturn's rings are omitted from the ground-based zonal averages. Measurements are colour-coded by date, according to the shared colour legend at the bottom of the figure. The location of local maxima in the zonal winds (eastward jets) are marked with vertical dotted lines following [García-Melendo et al. \(2011\)](#). The stratosphere is revealed by 7.8- μm observations, whereas 10.7, 17.6 and 18.6 μm sound the troposphere.

3.1. Synthetic Saturn images based on CIRS database

The time series of Saturn's atmospheric temperatures and stratospheric composition, retrieved from Cassini/CIRS between 2004 and 2017 (e.g., Fletcher et al., 2016, 2018b), was used to generate synthetic images of Saturn for comparison with ground-based data in Fig. 6. In this section we focus on COMICS observations in April 2005, and VISIR observations in September 2017. The latitude, longitude, and emission angle were extracted for every pixel in each image, such that viewing geometry and detector plate scales are properly accounted for. Latitude-pressure cross-sections of retrieved temperatures, ethane, and acetylene abundances were then used to generate synthetic radiances in each pixel, using the NEMESIS suite of radiative transfer and spectral retrieval tools (Irwin et al., 2008). Vertical and latitudinal profiles of CH₄, NH₃, and PH₃ were held fixed, and sources of spectral linedata (used to generate k -distributions for rapid calculations of spectral radiance) and collision-induced opacity are as described in Fletcher et al. (2018b). The k -distributions were convolved with filter profiles and telluric transmissions specific to each instrument, following (Fletcher et al., 2009b).

The calculated spectral radiance for each filter was used to assemble a synthetic image, which was then convolved with a wavelength-dependent Airy function (to represent diffraction) and a Gaussian (to represent the seeing). Noise was added to the synthetic to match that observed in the background surrounding Saturn, and the synthetics are compared to images in Fig. 6. The qualitative comparison is good, showing thermal banding and the increased emission of the SPSV (2005) and NPSV (2017) in the stratosphere, and even the compact polar cyclones (PCs) at 17.6 μ m.

We extract zonal-mean T_B profiles from both the synthetic images and the real data in Fig. 7 for a selection of five filters, averaging brightness within $\pm 30^\circ$ longitude of the central meridian. COMICS data in southern summer (blue-green) and VISIR data in northern summer (black-red) show agreement for all filters except 10.7 μ m (see below). The strong T_B gradients associated with Saturn's belts and zones are co-located in the CIRS-synthetic and the ground-based observations (see Section 3.2), except in regions where Saturn's rings begin to obscure the view from Earth. Polar brightness temperatures in both the troposphere and stratosphere are accurately reproduced by the CIRS synthetic. Furthermore, the ground-based T_B profiles are largely in the centre of the distribution of the CIRS T_B measurements, shown in the background of Fig. 7. We conclude from this comparison that the CIRS-derived temperatures and hydrocarbons are consistent with the COMICS and VISIR observations between 2004 and 2017, adding further validation to the CIRS results.

The one exception is the 10.7 μ m filter in Fig. 7(b), where the synthetic is not a good match to the observations. Although the observations are in a very dark region of Saturn's mid-IR spectrum, Fig. 7(b) nevertheless shows structure. The 10.7- μ m synthetic has more subdued banding than the data reveal, and the centre-to-limb variation of brightness does not match the observations. This filter senses the ~ 500 -mbar region of Saturn's troposphere, at depths where the far-IR CIRS focal plane was used to constrain atmospheric temperature. The downside of this was that the far-IR focal plane had a lower spatial resolution, and did not resolve belt/zone contrasts as well as the shorter-wavelength mid-IR CIRS focal planes (Flasar et al., 2004). Furthermore, 10.7 μ m spectral radiance depends on both the temperature structure and the distribution of PH₃. Due to an absence of published time-resolved CIRS PH₃ results, PH₃ was assumed to be uniform with latitude and time, which could have lessened the contrasts in the 10.7- μ m synthetic. Furthermore, the vertical distribution of PH₃ was not allowed to vary, which could cause the mismatch in the centre-to-limb brightness. The CIRS temperature and hydrocarbon record of Fletcher et al. (2018b) is therefore insufficient to reproduce ground-based observations at 10.7 μ m, and future modelling of Saturn's N-band spectrum (e.g., from the TEXES instrument mentioned in Section 2), alongside longer integration times at 10.7 μ m, will be required to improve on this mismatch.

3.2. Saturn's belts and zones

Observing Saturn with 8-m diameter mirrors provides sufficient spatial resolution to distinguish Saturn's thermal bands in the upper troposphere and stratosphere, as shown in Figs. 1 and 2. Latitudinal gradients in atmospheric temperature are related to the vertical shear on Saturn's zonal jets via the geostrophic thermal wind equation (e.g., Holton, 2004), and the decay of Saturn's zonal jets with altitude has been inferred via spectroscopic inversion using both Cassini (Flasar et al., 2005; Read et al., 2009; Fletcher et al., 2016) and Voyager data (Pirraglia et al., 1981). In this section, we show that the same conclusion can be reached via correlating brightness temperature contrasts from Subaru/COMICS during southern summer (2005 April 30) and VLT/VISIR during northern summer (2017 September 7). Note that a full temperature inversion will be performed in Section 3.3.

We used the highest-quality observations from both dates to generate calibrated equirectangular maps. A crude correction for limb-darkening/brightening effects was derived by sampling the brightness at all emission angles ($\mu = \cos \theta > 0.4$) within a restricted latitude range $\pm 10^\circ$ around the sub-observer latitude. This centre-to-limb effect was fitted with a fourth-order polynomial, which was then used as an empirical correction to the maps to remove the emission-angle dependence. An estimate of the zonal mean was derived by averaging within $\pm 30^\circ$ of the central meridian in each filter, and these are shown in Fig. 8 for both epochs.

To correct for the latitudinal dependence of the brightness temperature T_B on local gravity g and the Coriolis parameter $f = 2\Omega \sin \theta$, we followed Fletcher et al. (2021) in estimating a 'pseudo-shear' Δ on constant-pressure surfaces:

$$\Delta = -\frac{g}{fT_B} \frac{\partial T_B}{\partial y} \quad (1)$$

where y is the north-south distance. If we assume that the brightness temperature provides a good approximation to the kinetic temperature of the atmosphere at the peak of the contribution function for each filter, then this Δ can be viewed as a crude estimate of the vertical shear on the zonal winds, du/dz . The strong seasonal temperature contrasts in Saturn's troposphere and stratosphere produce significant trends in Δ as a function of latitude (such seasonal changes in windshear are quite valid and have been discussed elsewhere, e.g., Friedson and Moses, 2012). However, the purpose of this crude calculation is to identify the edges of Saturn's thermal bands, rather than to provide a quantitative estimate of the zonal winds at all altitudes, so we removed these seasonal trends via linear fitting between $15 - 70^\circ$ in each hemisphere, and subtracting it from the measured Δ . This adjusted form of Δ is shown in Fig. 8c-f, and is observed to oscillate back and forth around zero, giving a good indication of the boundaries of the thermal bands observed in the VISIR and COMICS images. We caution the reader that Δ should never be used quantitatively for zonal wind calculations as it lacks the seasonal temperature gradients, and that latitudes away from the sub-observer point will be viewed with lower spatial resolutions, such that Δ should be interpreted only as a qualitative guide to the edges of Saturn's thermal bands.

3.2.1. Temperate mid-latitudes

In Fig. 8c-f, we show how Δ compares to the peaks of the eastwards (prograde) and westwards (retrograde) cloud-top winds as measured by Cassini/ISS (García-Melendo et al., 2011). Focusing first on the temperate mid-latitudes ($30 - 70^\circ$ latitude in each hemisphere), Fig. 8 suggests that westward jets are associated with $\Delta > 0$ in all COMICS and VISIR filters, both in the troposphere (panel c-d) and stratosphere (panel e-f). However, for the eastward jets (which tend to be narrower), there are examples of both positive and negative Δ , although there is a clear trend for $\Delta < 0$ to be associated with strong eastward jets at mid-latitudes. Cassini/CIRS had previously shown this in the troposphere with true windshears of a similar magnitude (Fig. 16d of Fletcher

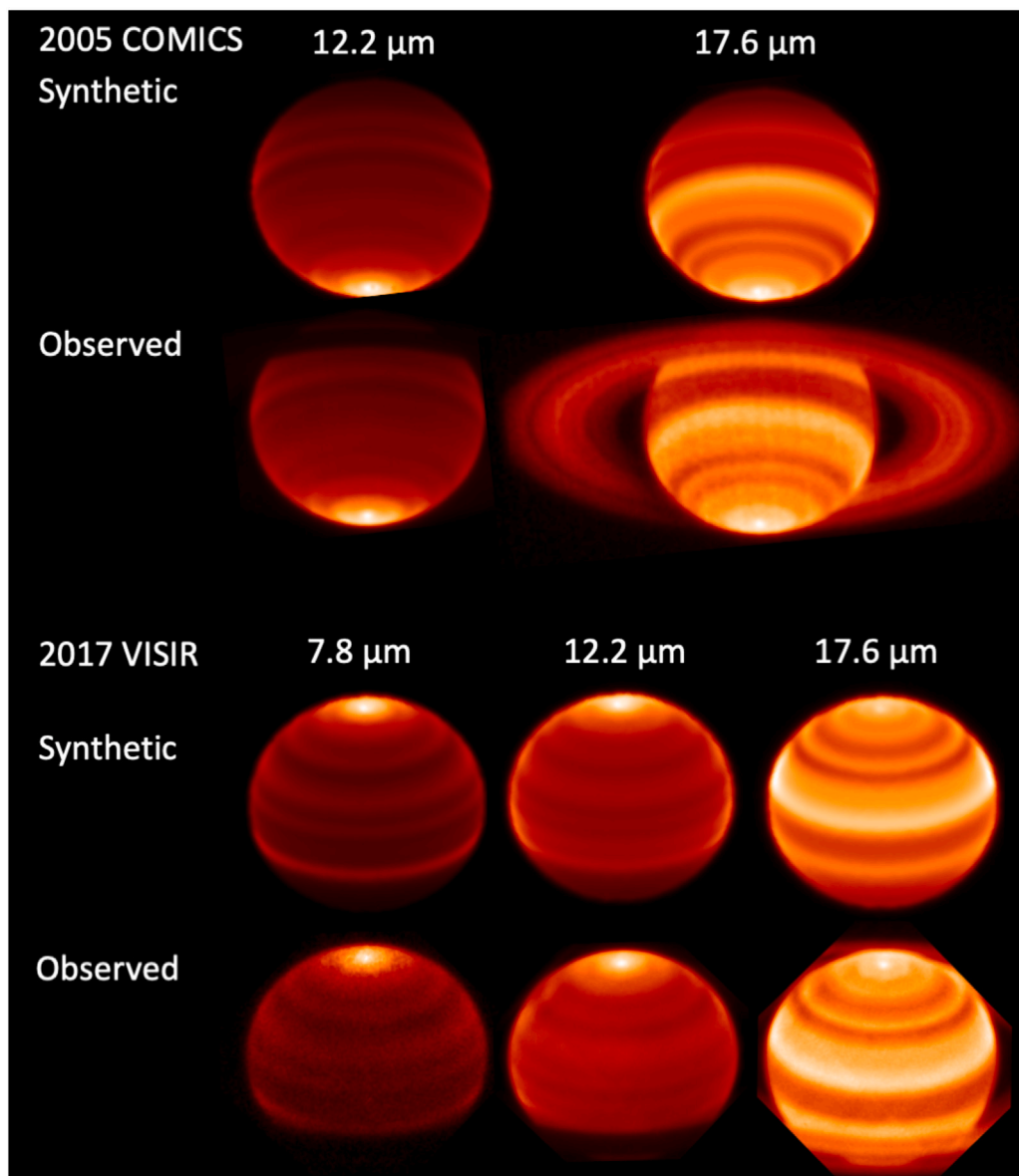


Fig. 6. Comparison of VISIR (September 2017) and COMICS (April 2005) observations of Saturn with synthetic images generated using the Cassini-derived record of temperatures and hydrocarbons, as described in the main text.

et al., 2016), but the stratosphere-sensing ground-based measurements at 7.9, 8.6–8.7, 12.3–12.5, and 13.0 μm in Fig. 8e, f reveal that this close correspondence also exists in the stratospheric brightness temperatures, indicating that the banded structure extends from the 500-mbar level to at least 1–10 mbar.

We assessed the strength of the correlation by calculating the Pearson correlation coefficient r_{xy} and their associated p -values, as shown in Fig. 9. We focused on Saturn's temperate mid-latitudes between $30 - 70^\circ$ so as to avoid bias from the strong equatorial jet (see below), and poor sampling of the polar regions. Moderate negative correlation between winds and the corrected pseudoshear of $r_{xy} = 0.75 \pm 0.1$ was observed in all filters, confirming that all mid-latitude zonal jets experience pseudoshear opposing their cloud-top motions. Fig. 9 suggests that this correlation is generally stronger in the troposphere-sounding filters than the stratosphere-sounding 7.9- and 11.6- to $-12.5\text{-}\mu\text{m}$ filters, but nevertheless remains significant in all cases. If this pseudoshear, which is based on brightness temperature rather than kinetic temperature, is a good estimate of the true windshear at the altitudes probed by each filter, then this confirms the weakening of the winds with altitude continues from the troposphere into the stratosphere.

The strong correlation between Saturn's mid-latitude jets and the latitudinal temperature gradients suggests that the banded structure of belts and zones is better defined by temperature and wind mapping than by the visible albedo (e.g., Vasavada et al., 2006). As on Jupiter, Saturn's eastward jets separate cool anticyclonic zones on their equatorward sides from warm cyclonic belts on their poleward sides, and this pattern persists throughout Saturn's temperate latitudes in both hemispheres. Evidence from aerosols and gaseous tracers, particularly NH_3 , PH_3 and para- H_2 (reviewed by Fletcher et al., 2020) suggest upwelling in zones and subsidence in belts, such that each zonal jet may be associated with a meridional circulation cell akin to the Earth's Ferrel cells (Del Genio et al., 2009; Fletcher et al., 2020), a phenomenon that is also at work on Jupiter (e.g., Duer et al., 2021). The VISIR and COMICS data presented here show how ground-based imaging can reveal thermal contrasts associated with Saturn's meridional circulation patterns on the scale of the zonal jets.

3.2.2. Tropical latitudes

The correspondence between tropospheric and stratospheric Δ becomes less clear at tropical latitudes within $\pm 30^\circ$ of the equator, where

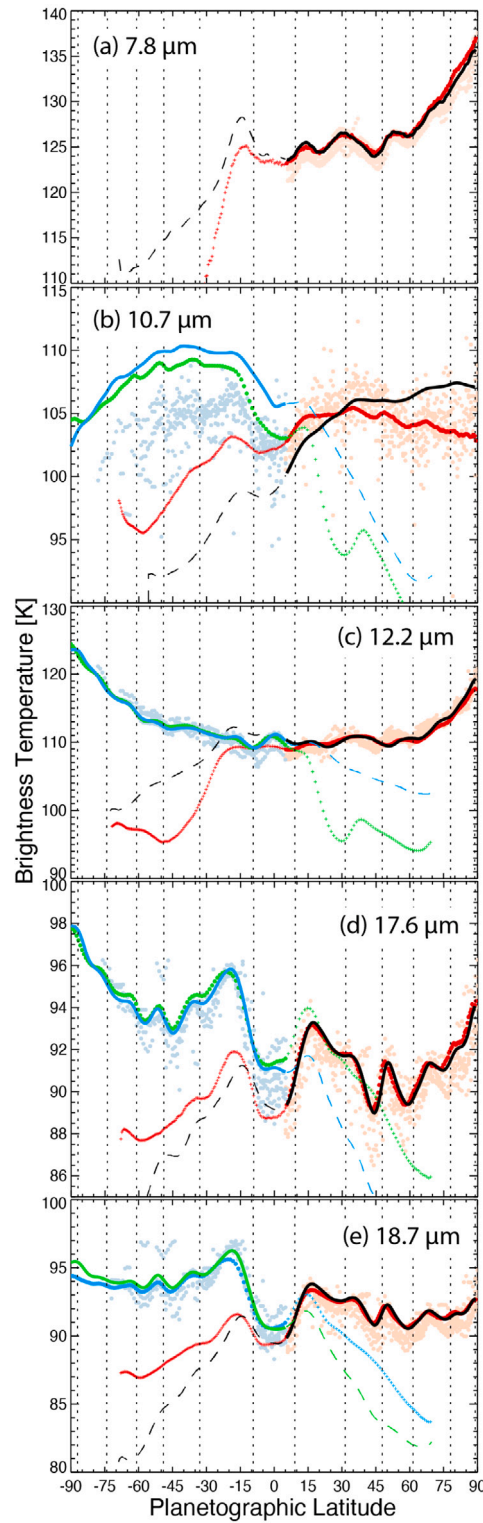


Fig. 7. Comparison of VISIR and COMICS brightness temperatures with CIRS-based synthetic images from Fig. 6. The September 2017 VISIR data (thick black) is compared with a synthetic profile (thick red) that is derived from the CIRS results. The dashed thin black line (data) and red crosses (synthetic, appearing as a thin red line) indicate regions obscured by Saturn's rings. Similarly, the 2005 COMICS profile (thick green line) is compared to the synthetic profile (thick blue), with the thinner dashed and crossed lines marking regions of ring obscuration. CIRS brightness temperatures are shown in the background as scattered points with colours matching the COMICS (2005, light blue) and VISIR (2017, light red) data. Neither COMICS nor VISIR data were available at 7.9 μm from 2005 for comparison in panel (a). The discrepancy at 10.7 μm is described in the main text. The latitudes of eastward maxima in the Cassini-derived wind field (García-Melendo et al., 2011) are marked as vertical dotted lines. (For interpretation of the references to colour in this figure legend, the reader is referred to the web version of this article.)

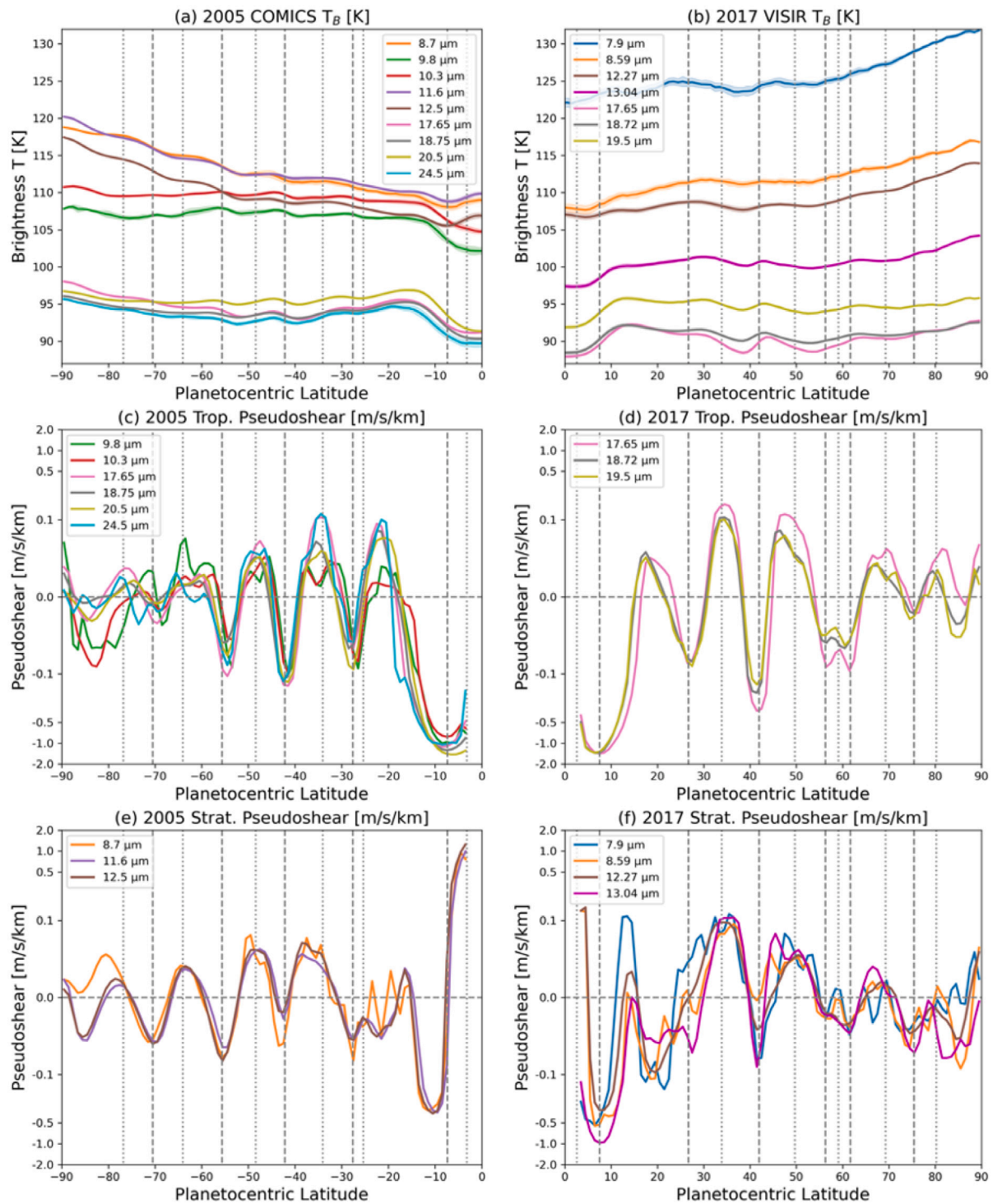


Fig. 8. (a, b) Zonally-averaged brightness temperatures observed during southern summer (April 2005 by COMICS, left) and during northern summer (September 2017 by VISIR, right). Vertical dashed lines indicate local maxima in the Cassini-derived wind field (eastward jets), vertical dotted lines indicate local minima (westward jets). Shaded regions represent the standard deviation of the zonal average, but do not include radiometric calibration uncertainties. Centre-to-limb variation has been approximately removed as described in the text. (c, d) Corrected pseudoshear for troposphere-sensing filters, estimated from the latitudinal T_B gradients as described in the main text, for 2005 and 2017, showing the correspondence of Saturn's thermal gradients and the wind field. (e, f) show corrected pseudoshear for stratosphere-sensing filters. Note that the y-axis scale is linear within ± 0.1 m/s/km, and logarithmic thereafter. Pseudoshears are not shown within $\pm 3^\circ$ of the equator, where the Coriolis parameter f tends to zero. (For interpretation of the references to colour in this figure legend, the reader is referred to the web version of this article.)

Saturn's wind field is dominated by the broad eastward jet (García-Melendo et al., 2011). For example, the eastward jet at 27°N coincides with $\Delta < 0$ for troposphere-sounding filters (13.0–19.5 μm in Fig. 8c, d), but $\Delta > 0$ for stratosphere-sounding filters (7.9, 8.6 and 12.3 μm , Fig. 8e, f), indicating that Δ changes direction at altitudes above the tropopause. Intriguingly, this is not seen for the mirror-jet at 29°S, where all the images have $\Delta < 0$. Another example are the small maxima in the winds at $\pm 7.5^\circ$ (planetocentric), which are superimposed onto Saturn's broad equatorial jet. These are associated with strong negative pseudoshear near $\pm 10^\circ$ in the troposphere-sounding filters, but the stratosphere-sensing filters are notably different in Fig. 8e, f.

These low-latitude pseudoshears are likely to be temporally variable, particularly in the stratosphere. In 2005 and 2017, Δ remained negative for the troposphere-sensing filters (17–19 μm) throughout the $0 - 15^\circ$ region (i.e., the equatorial zone is cold). Conversely, the stratospheric filters (8.7, 11.6 and 12.5 μm for COMICS; 7.9, 8.6, 12.27 and 13.04 μm for VISIR) show positive Δ equatorward of 7.5° in 2005 (Fig. 8e), but remain negative in 2017 (Fig. 8f). This difference is likely associated with the equatorial contrasts driven by Saturn's stratospheric oscillation. The equatorial maximum was stronger in 2005 than in 2017, but as only ~ 12 years had elapsed between these observations, compared to the ~ 15 -year period of Saturn's equatorial oscillation (Orton et al., 2008), we may be at an earlier stage of the warming at 1–10 mbar. This is consistent with the findings of Fletcher et al. (2017), but see Section 5 for discussion of this progression beyond 2017.

3.2.3. Polar latitudes

Poleward of 70° in both hemispheres, Fig. 8c–f shows weaker correspondence between Δ and the zonal jets. Eastward jets at 71°S and 76°N (i.e., the latitude of Saturn's hexagon) show local minima in Δ in both the troposphere and stratosphere, and there are hints of $\Delta < 0$ in the latitude domain surrounding the SPC in 2005 (87°S) and the NPC in 2017 (86°N), i.e., the strength of the cyclonic vortices decays with altitude. Nevertheless, these polar gradients are more scattered than at mid-latitudes, likely because the magnitude of Δ is extremely sensitive to the spatial resolution of the polar T_B measurements in Fig. 8a–b.

3.3. Temperature retrieval

As a final demonstration of the capabilities of 8-m facilities to constrain the thermal structure of Saturn's atmosphere, we perform a crude spectral inversion of the April-2005 COMICS observations and September-2017 VISIR observations to estimate the 2D (latitude-pressure) temperature structure, in Fig. 10. A single latitude-independent temperature profile (a low-latitude average from Fletcher et al., 2009a) was used as the *a priori* for retrievals at all latitudes and epochs. The COMICS inversion repeats that shown in Fig. 14 of Fletcher et al. (2009b), and includes the significant uncertainties inherent in retrievals from stacks of 7–9 narrow-band images spanning 7–25 μm . This is an under-constrained problem, with a small number of spectral points being used to determine a smoothed $T(p)$ structure, using observations that have been calibrated by scaling to Cassini/CIRS. Furthermore, the two inversions possess differing information content: the 2005 COMICS inversion lacks a filter sensing stratospheric CH_4 at 7.9 μm ³. The stratospheric temperatures were therefore primarily controlled by the COMICS 12.5- μm filter, which senses C_2H_6 (a latitude-independent C_2H_6 vertical profile was used as the prior, based on Fletcher et al., 2018b). Similarly, the VISIR inversion lacks deeper-sounding N-band observations at 9–11 μm , such that the 2017 tropospheric temperature are controlled only by the 13–19 μm filters.

Formal retrieval errors range from ~ 1.5 K at 500 mbar, to ~ 2.0 K at 100 mbar, to ~ 3.5 K at 1 mbar. The absolute temperatures at each level are therefore rather uncertain, but Fig. 10 does serve to show

(i) the seasonal trends in hemispheric temperatures near southern and northern solstice; and (ii) the modulation of the temperatures by the belt/zone structures associated with the shear on the zonal winds (Section 3.2). At 1 mbar, the peak temperatures within the SPSV (~ 162 K) and the NPSV (~ 150 K) are within ± 5 K of the temperatures measured by Cassini/CIRS during the same periods (Fletcher et al., 2018b). At 110 mbar, the temperature estimates during southern summer (90 ± 2 K) and northern summer (86 ± 2 K) are consistent with those derived from Cassini/CIRS (Fletcher et al., 2018b). This is not surprising, given the use of CIRS data to calibrate the ground-based data, but demonstrates the self-consistency of this approach.

4. Saturn's seasons before Cassini

The high-resolution ground-based record of Saturn's tropospheric and stratospheric temperatures described in Section 3 spans slightly less than half a Saturnian year, from 2004 to 2017. However, lower-resolution images of Saturn's mid-infrared emission (Gezari et al., 1989; Orton et al., 2008) extend back to the 1980s. In particular, observations from NASA's Infrared Telescope Facility (IRTF) span the previous northern spring (June 1984, $L_s = 50^\circ$, to December 1987, $L_s = 90^\circ$), northern summer ($L_s = 90 - 180^\circ$, until November 1995), and northern autumn ($L_s = 180 - 270^\circ$, until October 2002). In Section 4.1 we present this longer-term time series, and generate synthetic images based on Cassini-era temperature and hydrocarbon distributions to search for evidence of interannual variability. Then in Section 4.2 we compare the mid-IR observations to numerical radiative-convective models (Guerlet et al., 2014) and radiative-photochemical models (Hue et al., 2016).

4.1. Inter-annual variability

Fig. 11 displays annual zonal-mean brightness temperatures for two filters sensing stratospheric CH_4 (7.8–8.0 μm) and C_2H_6 (12.2–12.5 μm). This figure extends that of Orton et al. (2008), and the averages are extracted from a longitude range within $\pm 30^\circ$ of the central meridian from images such as those shown in Figs. 1–4. As the quality of the mid-IR imaging has improved significantly over the past four decades, a quantitative comparison of the observations is challenging: for example, the visibility of the banded structure and warm polar vortices varied considerably as spatial resolution and detector sensitivity has improved. Lower spatial resolutions blend Saturn's limb emission with the surrounding dark sky, artificially darkening the limb and moving the brightest polar emission to lower latitudes (e.g., the peak often occurs near 75°N in the 1984–1993 datasets in Fig. 11). Nevertheless, Fig. 11 displays qualitative trends: (i) the seasonal progression of the hemispheric asymmetry, warming in the spring and cooling in the autumn; (ii) the peak emission from the summertime poles as the North/South polar stratospheric vortices (NPSV, SPSV) form (Fletcher et al., 2018b); and (iii) the change in low-latitude temperature contrasts associated with Saturn's equatorial stratospheric oscillation (Orton et al., 2008). We shall return to each of these points below.

Given the proposed semi-annual nature of the equatorial oscillation (Orton et al., 2008; Fouchet et al., 2008), our first-order assumption would be that Saturn should appear the same from one Saturnian year to the next. Thus temperatures measured by Cassini/CIRS near the end of the mission ($L_s = 93^\circ$, September 2017) should provide a good approximation to the first 2D thermal images of Saturn observed one Saturnian year earlier (March 1989, $L_s = 103^\circ$, Gezari et al., 1989). The exact anniversary of $L_s = 103^\circ$ was August 2018, after the end of the Cassini mission. Using the technique described in Section 3.1, we generated synthetic images in Fig. 12 to match the observations of Gezari et al. (1989), using the platescale and field-of-view of the 2D camera in 1989, but using the temperatures and hydrocarbon distributions from Cassini measurements in 2017. The filter functions of the original IRTF camera are not available, so we used Gemini/Michelle filter functions as a substitute for the three filters (Glasse et al., 1997).

³ A 7.9- μm filter was later added to the COMICS instrument.

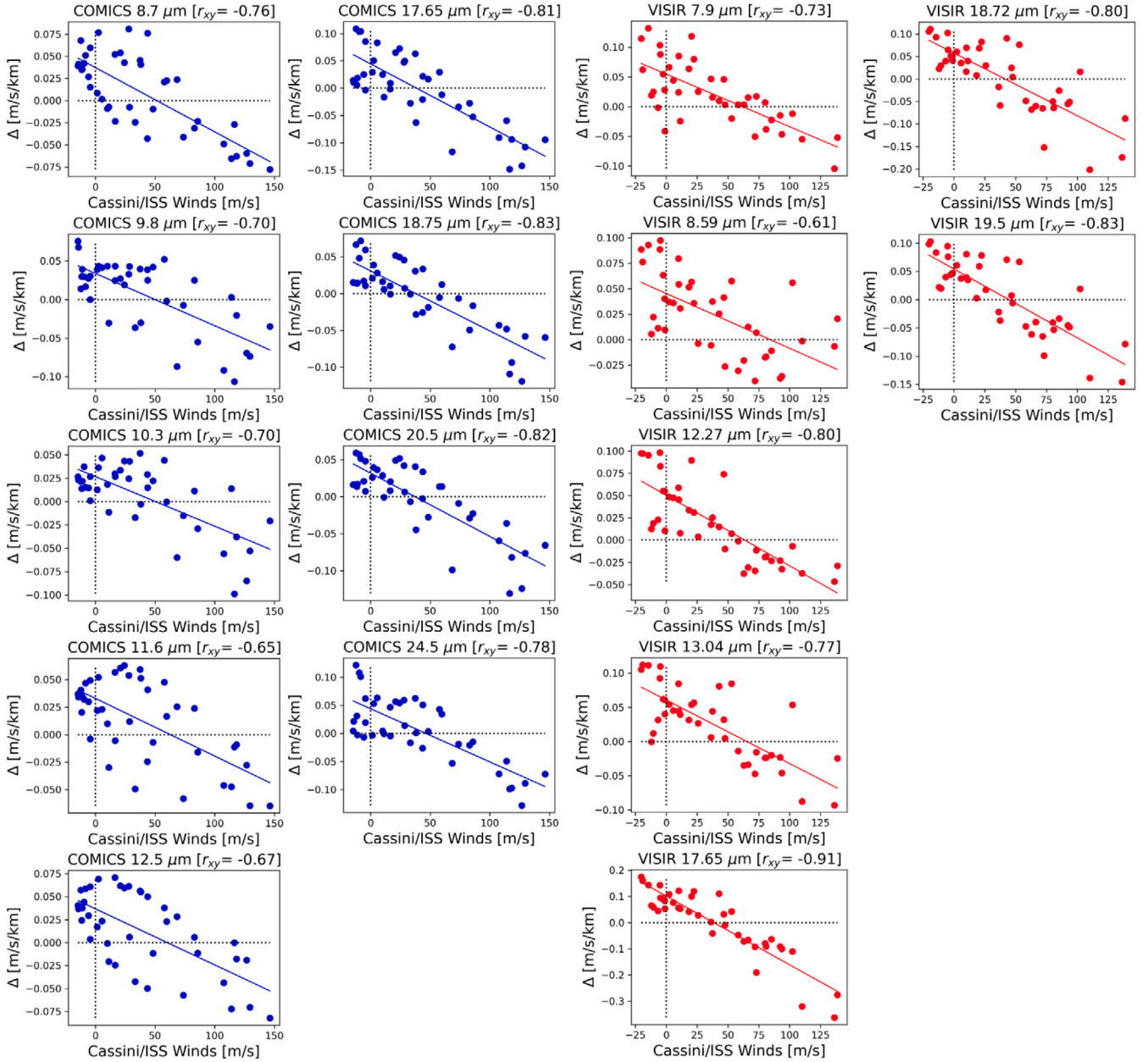


Fig. 9. Negative correlation between Cassini-derived cloud-top winds of [García-Melendo et al. \(2011\)](#) and the pseudoshear Δ , measured in the $30 - 70^\circ$ latitude range for each hemisphere. Left columns show the correlation during southern summer in blue (April 2005, COMICS), right columns show the correlation during northern summer in red (September 2017, VISIR). Pearson correlation coefficients r_{xy} are provided for each panel, along with a linear regression line. (For interpretation of the references to colour in this figure legend, the reader is referred to the web version of this article.)

The synthetic images and data are shown in [Fig. 12](#), and are compared to VISIR observations in May 2018, close to the anniversary of the 1989 observations.

[Fig. 13](#) directly compares the synthetic images with the calibrated 1989 observations at $7.8 \mu\text{m}$, $11.6 \mu\text{m}$ and $12.4 \mu\text{m}$. We sampled the brightness temperatures through the same longitude as ([Gezari et al., 1989](#)); 20° east of the central meridian. While the comparison is reasonable, with the warm polar domain $> 70^\circ\text{N}$ observed in all three filters, the detection of the same warm mid-latitude band near 30°N at $7.8 \mu\text{m}$, and predicted temperatures within the range of uncertainty in the calibration of the [Gezari et al. \(1989\)](#), there remain some structural differences. The rapid drop in brightness temperature south of 15°S is due to absorption from Saturn's rings at 11.6 and $12.4 \mu\text{m}$. Ethane emission at $12.4 \mu\text{m}$ appears to be systematically brighter than the Cassini prediction in the northern hemisphere by $\sim 4 \text{ K}$, but this is

likely due to challenges in filter calibration and uncertainties associated with the filter function, as temperature offsets are not seen at 7.8 and $11.6 \mu\text{m}$. However, close inspection of maxima and minima in the 11.6 - and $12.4\text{-}\mu\text{m}$ latitude profiles suggest latitudinal offsets in the location of warm bands. Mid-latitude differences between 2017 and 1989 could be real, given thermal and chemical consequences of the 2010 northern springtime storm ([Fletcher et al., 2012](#); [Moses et al., 2015](#)). However, mid-latitude stratospheric perturbations from the storm had largely dissipated by 2017 ([Fletcher et al., 2017](#)), and the temperature-dependent photochemistry within the 'beacon' should not have significantly affected the C_2H_6 abundance ([Moses et al., 2015](#)). The apparent differences in the $15 - 60^\circ\text{N}$ domain may not be genuine, given the difficulties of navigating the precise location of the limb in the 1989 images.

The most robust difference between the 1989 observations and the Cassini-epoch predictions is at low latitudes at $7.8 \mu\text{m}$. Both the

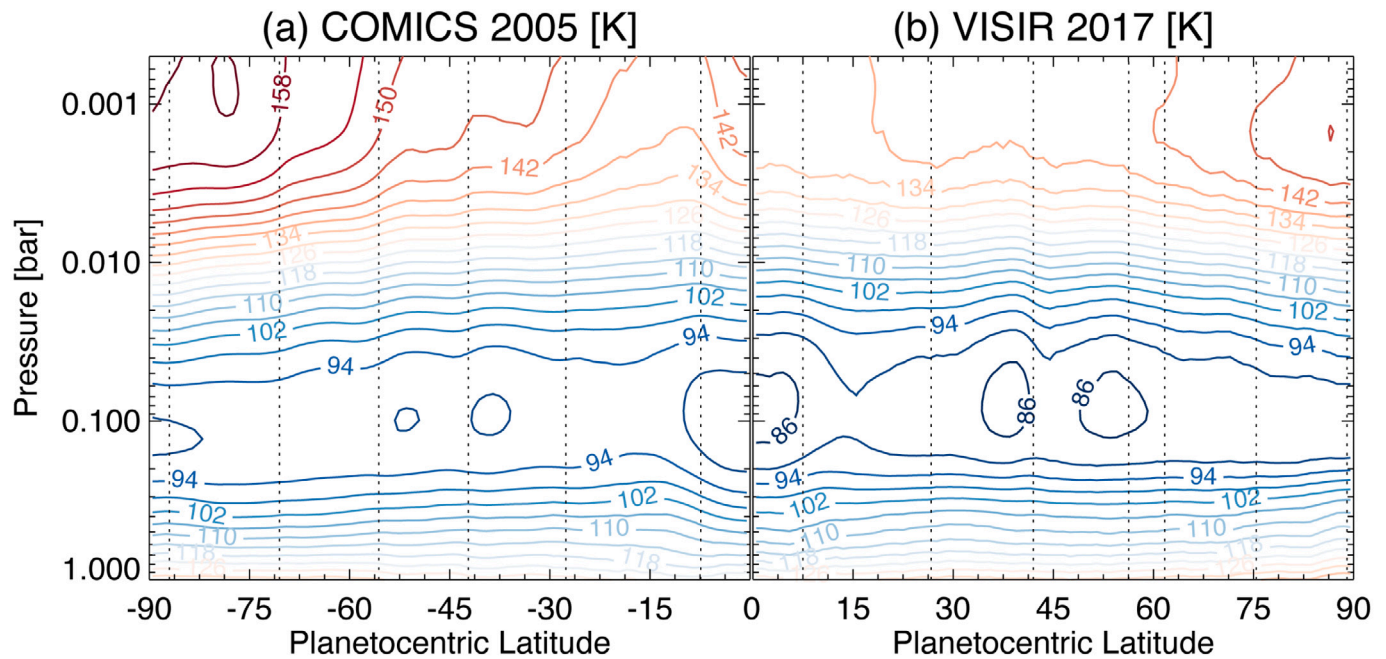


Fig. 10. Temperature cross-sections during southern summer (left, derived from COMICS in April 2005, Fletcher et al., 2009b) and northern summer (right derived from VISIR in September 2017). Spectra formed from stacking the available filters in Fig. 8 were inverted to provide a crude estimate of the temperature, with uncertainties ranging from ~ 1.5 K at 500 mbar, to ~ 2.0 K at 100 mbar, to ~ 3.5 K at 1 mbar. Vertical dotted lines show the locations of the prograde eastward jets at the cloud tops.

1989 images in Fig. 12 and the zonal average in Fig. 13 display a warm equatorial band at $7.8 \mu\text{m}$. This warm band is not present in our synthetic images in Fig. 12b (based on 2017 CIRS data), nor in the May-2018 VISIR observations in Fig. 12c. This warm equatorial band could also have been present in $7.8\text{-}\mu\text{m}$ images before 1989, but the low spatial resolution and high uncertainty on these early images in Fig. 3 make it hard to be conclusive. The warm band can be seen in the 1990 images in Fig. 3, albeit at low contrast because of the warmer belt immediately north of the equator. This is consistent with Fig. 3 of Orton et al. (2008), which suggests a peak in the equatorial brightness near northern summer solstice.

Fig. 11a reveals that the warm band was absent through the 1990s, but could be seen again in IRTF and Keck imaging in 2002–2004 (Fig. 1, Orton and Yanamandra-Fisher, 2005), throughout 2007–2013 images from COMICS and VISIR in Fig. 1, but COMICS and VISIR images between 2015 and 2020 (Fig. 2) shows that the equator was cooler throughout this epoch. Unlike the CH_4 sensing filter, a warm equatorial band has been observed at $12.2\text{--}12.5 \mu\text{m}$ throughout the 2007–2020 period, suggesting that this filter sounds a deeper level of the equatorial oscillation.

The local minimum in equatorial $7.8\text{-}\mu\text{m}$ brightness temperature near northern summer solstice in 2017 is also seen in the Cassini/CIRS brightness temperatures (Fig. 5A), so it is no surprise that our Cassini-epoch predictions of 1989 brightness temperatures expects a local equatorial minimum in Fig. 13a. If the equatorial stratospheric oscillation were truly semi-annual at this altitude (10 mbar), then we would expect the oscillation to display the same latitudinal contrasts one Saturnian year apart. Saturn's tropical stratosphere therefore displays inter-annual variability, as the equatorial stratospheric oscillation is not semi-annual. The ~ 15 year period has been questioned previously: Sinclair et al. (2014) found that 2.1-mbar temperatures derived from Cassini/CIRS in 2009–10 showed a local temperature maximum (consistent with our VISIR images in Fig. 1), whereas those derived from Voyager/IRIS in 1980 (one Saturnian year earlier) showed a local temperature minimum. The sinusoidal oscillation envisaged in Fig. 3 of Orton et al. (2008) does not seem to have held after ~ 2006 , meaning that equatorial temperature contrasts from the Cassini epoch are not a good model for the brightness in the 1980s.

Natural variability in equatorial oscillations is not unexpected. No terrestrial equatorial oscillation, neither the quasi-biennial oscillation (QBO) nor the semi-annual oscillation (SAO), has a perfectly fixed period, and Earth's QBO has been disrupted in the recent past (Osprey et al., 2016). Saturn's equatorial oscillation was disrupted for a period of ~ 3 years, when a large warm stratospheric vortex was present, related to the northern springtime storm (Fletcher et al., 2017). The contemporaneous nature of these two phenomena suggested momentum transfer by waves from Saturn's mid-latitudes to the equator, but this has yet to be confirmed via numerical modelling. Jupiter's equatorial oscillation also appeared to shift periods as a consequence of global-scale changes in the planetary bands (Giles et al., 2020; Antuñaño et al., 2021). Thus equatorial oscillations can vary with time due to variable activity in the troposphere, such as extreme weather events or other wave-generating phenomena, which alter the wave-mean flow interactions. The period of these oscillations also vary with height, as the vertical propagation of the waves that force the equatorial winds is not always the same, meaning that the altitude of wave-breaking constantly changes. Saturn's equatorial oscillation could therefore be viewed as a hybrid of a QBO-like phenomenon (i.e., the descent of zonal shear zones towards the tropopause, driven by variable activity in the troposphere) and a seasonally-forced phenomenon, where the phase of the oscillation is naturally variable. Furthermore, the time span of our observations remains insufficient to properly define the 'mean' period and properties of Saturn's oscillation.

Considering Fig. 11a and the images in Figs. 1–4, which show warm $7.9\text{-}\mu\text{m}$ bands evident in 1989–1990 and 2004–2010, and minima evident in 1996–2000 and 2015–2020, might suggest that a longer-term oscillation with a ~ 20 -year period could be more appropriate than the $\sim 14\text{--}16$ years typically quoted. This would help to explain why observations taken one Saturnian year apart are not in phase with one another, as shown by this work and Sinclair et al. (2014). However, VISIR observations in 2021 and 2022 indicate the re-emergence of the warm $7.9\text{-}\mu\text{m}$ band, $\sim 15\text{--}17$ years after its last peak in 2004–2006, so the period remains considerably uncertain. The existence of the local equatorial minimum in Fig. 2 between 2015 and 2020 could be a continued consequence of Saturn's 2010 storm, but this cannot explain why IRIS (1980) and CIRS (2009) observations near equinox were

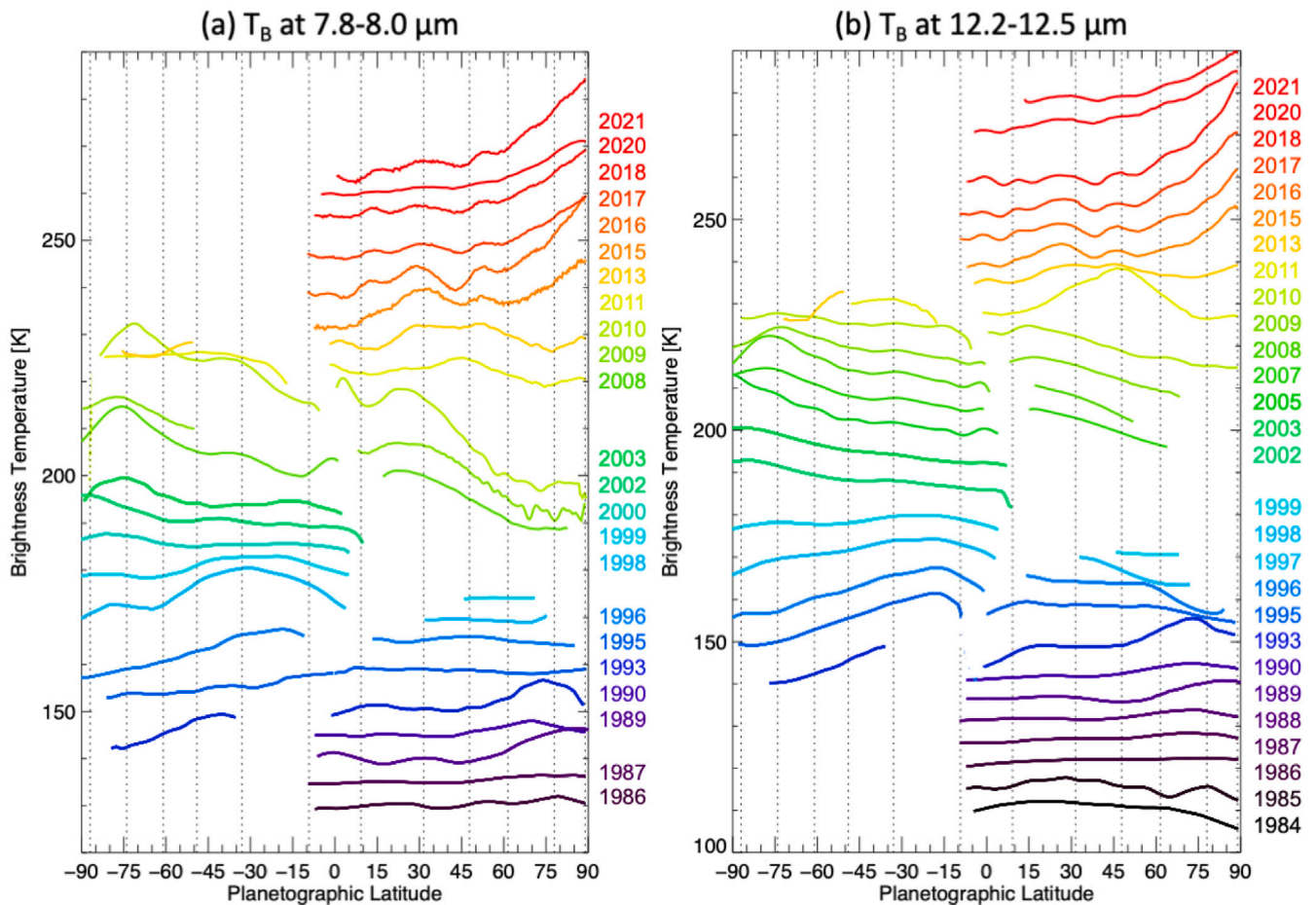


Fig. 11. Zonal-mean stratospheric brightness temperatures (CH_4 emission near $8\ \mu\text{m}$, and C_2H_6 emission near $12.3\ \mu\text{m}$) extracted from selected observations from 1984 to 2021. Temperature profiles are offset from the earliest date by multiples of 5 K for clarity, and colour-coded by year. Dotted lines show the location of Saturn's eastward jets. Standard deviations on zonal averages are less than 0.5 K, but this does not include systematic calibration uncertainties. Regions of ring obscuration are omitted. Given the significant improvement in image quality from 1984 to 2021, this comparison should be treated with caution, as described in the main text. In particular, the bright polar emissions in the 1980s datasets often appear near $\sim 75^\circ\text{N}$ rather than right at the pole, due to the coarse spatial resolution of the earliest datasets.

apparently out of phase. The September 1990 storm (Sánchez-Lavega et al., 1991) is unlikely to be the cause, given that the equatorial oscillation appeared to be well-behaved between 1990–2005 in the study of Orton et al. (2008). Continued long-term monitoring of Saturn's equatorial oscillation will be needed to better constrain its periodicity, and whether the warm equatorial $7.9\text{-}\mu\text{m}$ band continues to re-establish itself in the years to come.

4.2. Comparison with radiative models

With the exception of the variability associated with the equatorial oscillation, and the strong emission from the northern storm 'beacon' in 2011–2014, the ~ 37 -year time series in Fig. 11 suggests a slow seasonal reversal in hemispheric contrasts associated with radiative heating and cooling. In this section we compare the observations with predictions based on the radiative climate models of Guerlet et al. (2014) and Hue et al. (2016).

SPIICE software tools provided by the Navigation and Ancillary Information Facility (NAIF, Acton, 1996), accessed via 'Spiceypy' (Annen et al., 2020), were used to calculate Saturn's ephemerides at all oppositions (as viewed from Earth) between 1980 and 2030. For each opposition, visible latitudes, longitudes, illumination and viewing angles were projected onto the sky using the 0.045 arcsecond-per-pixel grid of VISIR. These were extracted along the central meridian on a $0.25''$ grid. For each latitude and L_s , we interpolated and extracted the relevant $T(p)$ from the model of Guerlet et al. (2014), or the relevant

$T(p)$ and ethane/acetylene distributions from the model of Hue et al. (2016). We compare the results from both models, as they used slightly different assumptions: Guerlet et al. (2014) hold hydrocarbon distributions fixed with time, whereas Hue et al. (2016) iterate between a radiative model and photochemical model, allowing the distribution of the stratospheric coolants to change with time. These subtle differences in hydrocarbon distributions have a secondary impact on the predicted brightness temperatures, which are primarily governed by the modelled stratospheric temperatures.

Spectral radiance was forward-modelled in each VISIR filter (7.9 – $20\ \mu\text{m}$) for each central meridian position and date, providing a prediction of the brightness temperature variation as a function of time. The results are shown in Fig. 14 for three filters: $7.9\ \mu\text{m}$ sensing stratospheric CH_4 , $12.3\ \mu\text{m}$ sensing stratospheric C_2H_6 , and $17.7\ \mu\text{m}$ sensing tropospheric H_2 . Ring-obscured latitudes have not been removed. It is important to note that neither model was designed to produce the fine-scale belt/zone structure visible in Saturn's atmosphere, nor the pattern of equatorial stratospheric variability (Orton et al., 2008; Fletcher et al., 2017). Systematic discrepancies in the absolute temperatures predicted by the models and measured by CIRS are discussed extensively by the authors (Guerlet et al., 2014; Hue et al., 2016). Nevertheless, the radiative models are remarkably consistent with one another, and provide a useful prediction of the timings of peak temperatures (and hydrocarbon abundances). The forward models in Fig. 14 simply translate these into predicted brightnesses, based on the visibility and emission angles for each latitude.

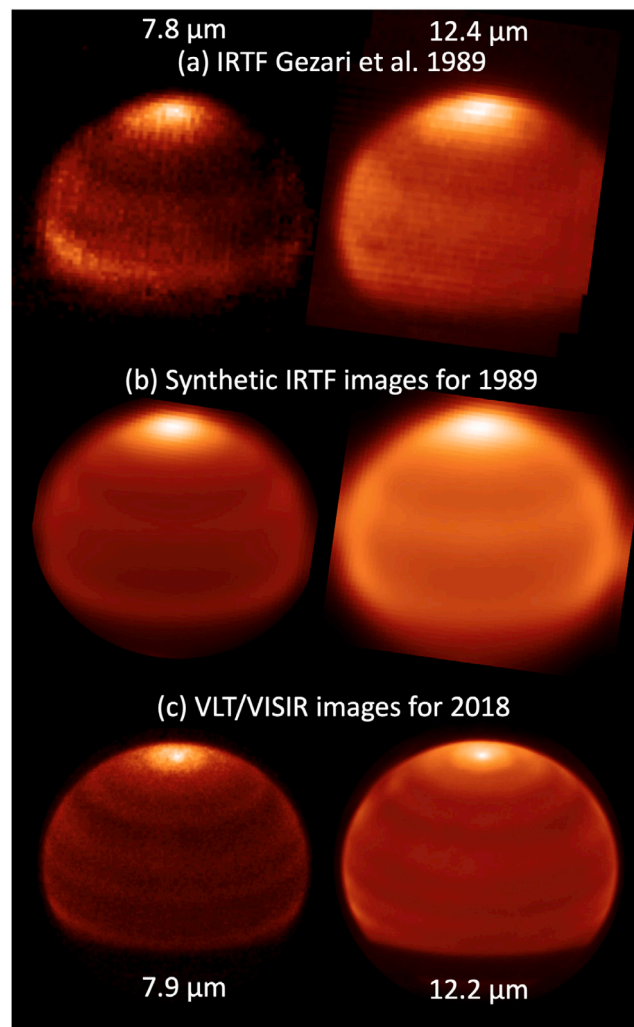


Fig. 12. Comparison of synthetic images (b) based on the March-1989 ($L_s = 104^\circ$) observations of Gezari et al. (1989) using a 3-m mirror (a). These can be compared to VLT/VISIR observations from May 2018 ($L_s = 101^\circ$), at approximately the same moment in Saturn's seasonal cycle.

Fig. 14 reveals that both models reproduce the observed brightening of the summertime poles, and that this peak brightness is offset from the solstices. At $7.9 \mu\text{m}$, the temperatures are expected to be relatively uniform along the central meridian in ~ 1983 and ~ 2013 in the northern hemisphere, and ~ 1998 in the southern hemisphere. A gradient in brightness then becomes established (the pole being warmer than the sub-observer point), peaking around 1991 and 2020 for the north pole in both models. This peak brightness is 3–4 years after summer solstice, due to (i) the lagged warming of the stratosphere predicted by the models, and (ii) the fact that the warmest polar latitudes come close to the limb after solstice, their brightness being enhanced by limb brightening. Furthermore, both models predict a warmer southern-summer peak $7.9 \mu\text{m}$ emission than for the northern summer, as a consequence of closer proximity to the Sun (perihelion). The difference in angular size of Saturn from aphelion to perihelion can be readily seen in Fig. 14. With ground-based observations it is then hard to track the subsequent cooling, as the high autumnal latitudes appear to recede from view faster than the predicted polar cooling.

Both models predict that the north polar region should be brightest in 2020–21 in all three filters, and that future measurements should show a decline. But what about the previous Saturnian summers? The brightness contrast for the north polar region can be seen in Fig. 11. Gezari et al. (1989) should have been taking observations during the warmest epoch for the north pole in 1989–1990, as shown in Fig. 3, and the warm NPSV remained visible in 1993 and 1995 MIRAC2

observations in Fig. 4. Observations by MIRLIN and SPECTROCAM10 in 1996 ($L_s = 190^\circ$, shortly after equinox) reveals the absence of any bright polar emission at 7.9 and $12.3 \mu\text{m}$. This is counter to the expectations of both models in Fig. 14, which suggest that a weak positive gradient from the disc-centre to the north pole should persist to the late 1990s. The data imply that the north polar region cools faster than predicted by either model — we speculate that enhanced radiative cooling by aerosols, photochemically produced during the maximum illumination of summer, might account for this discrepancy. However, this could also be a consequence of poorer spatial resolution during the 1990 observations of northern autumn, as the VISIR observations of southern autumn (Fig. 1) show the persistence of bright south-polar emission until 2010, consistent with the radiative models.

What about the onset of polar brightening in Saturnian spring? Both the $12.4\text{-}\mu\text{m}$ data in Fig. 3 and the model suggest the first occurrence of bright north polar emission between 1984–1985 ($L_s = 45^\circ - 70^\circ$). During the Cassini epoch, the north polar emission is predicted to have become visible after ~ 2014 ($L_s \sim 60^\circ$), within the 2011–15 gap in our time series between Fig. 1 and 2, but consistent with the findings from Cassini/CIRS (Fletcher et al., 2018b). During southern spring, the first hints of a warm south pole were observed at $7.8 \mu\text{m}$ by MIRLIN in 2000 ($L_s = 233^\circ$, Fig. 4), consistent with the predictions of the radiative model. This bright south polar emission was also observed by Keck in 2004, just prior to Cassini's arrival (Orton and Yanamandra-Fisher, 2005).

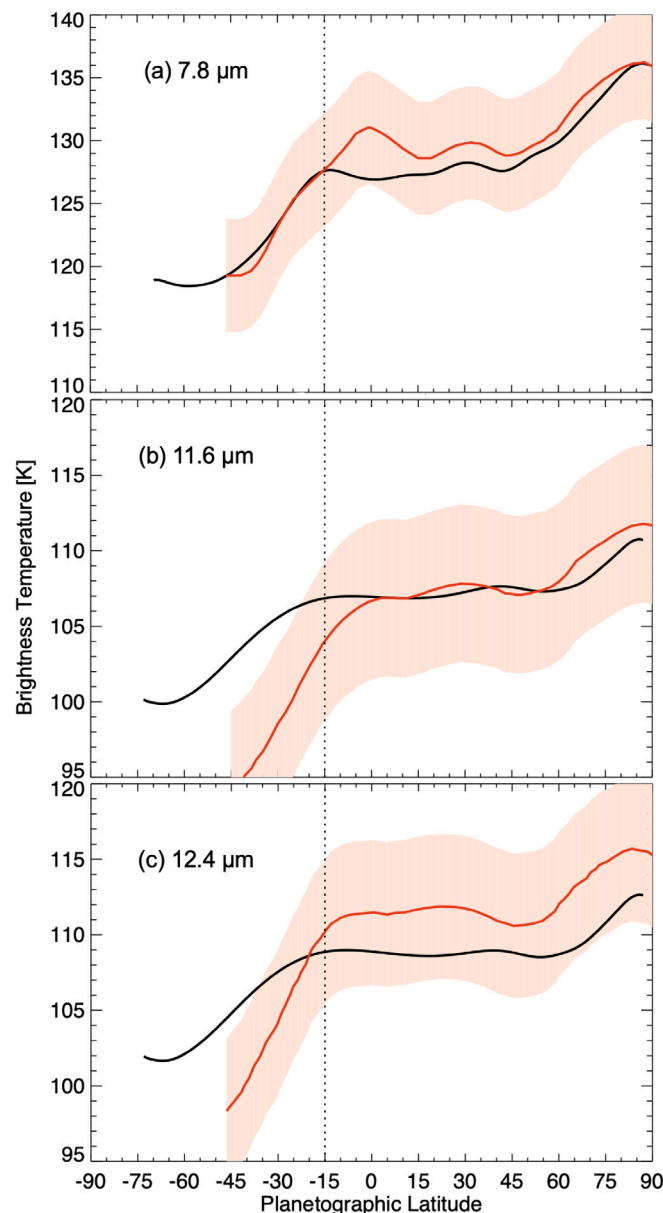


Fig. 13. Comparison of Saturn's zonally-averaged brightness in March 1989 (red curve, [Gezari et al., 1989](#)) with scans extracted from synthetic images (black curve) at 7.8 μm , 11.6 μm and 12.4 μm . Regions southward of the vertical dotted line (black) are obscured by the rings. Absolute uncertainties on the brightness temperatures (shaded regions) are estimates from the standard deviation of the background in the 1989 images. Although these are large compared to the measured zonal contrasts, the relative variability is consistent with that shown in [Fig. 12\(a\)](#). (For interpretation of the references to colour in this figure legend, the reader is referred to the web version of this article.)

Given that [Hue et al. \(2016\)](#) also consider photochemical variations with time, we might have expected larger differences between the two models in [Fig. 14](#). Stronger latitudinal gradients in 7.9- and 12.3- μm emission are present in the [Hue et al. \(2016\)](#) model, and although these are closer to the observations, the absence of circulation makes the comparison challenging. Furthermore, there is a subtle shift in the timing of the maximum brightness by approximately 1 year, closer to solstice for the model of [Hue et al. \(2016\)](#). Neither the 1985–95 nor the 2015–2020 datasets have sufficient temporal sampling to reliably distinguish between these models. We return to the question of variability in the 2015–2022 observations in Section 5.

Finally, we note that neither model does a good job at reproducing the tropospheric brightness. Both predict an equatorial maximum temperature following the annually-averaged insolation, whereas in fact the observed temperatures in [Figs. 1 and 2](#) are more uniform, albeit with the belt/zone variability superimposed on top. Nevertheless, the radiative models predict the existence of brighter polar emission at

17.7 μm that is consistent with the data, which show a brighter south polar emission between 2003–2009, and north pole between 2017–2020, and in 1990. The data from 8-m facilities in [Figs. 1–2](#) show this brightness to be entrained poleward of approximately $\pm 75^\circ$ latitude, along with contributions from the compact polar cyclones.

In summary, despite the problems at low latitudes and systematic differences in temperature, the models consistently reproduce the bright polar emission observed in the data, correctly predicting the onset of bright emission in springtime, and the disappearance of the bright emission in autumn.

5. Saturn after the Cassini mission

Since the demise of Cassini in September 2017, ground-based facilities (including VLT/VISIR and Subaru/COMICS) have continued to track Saturn's mid-infrared emission. VLT/VISIR was inaccessible in 2019–20, and Subaru/COMICS was decommissioned in 2020 (planned

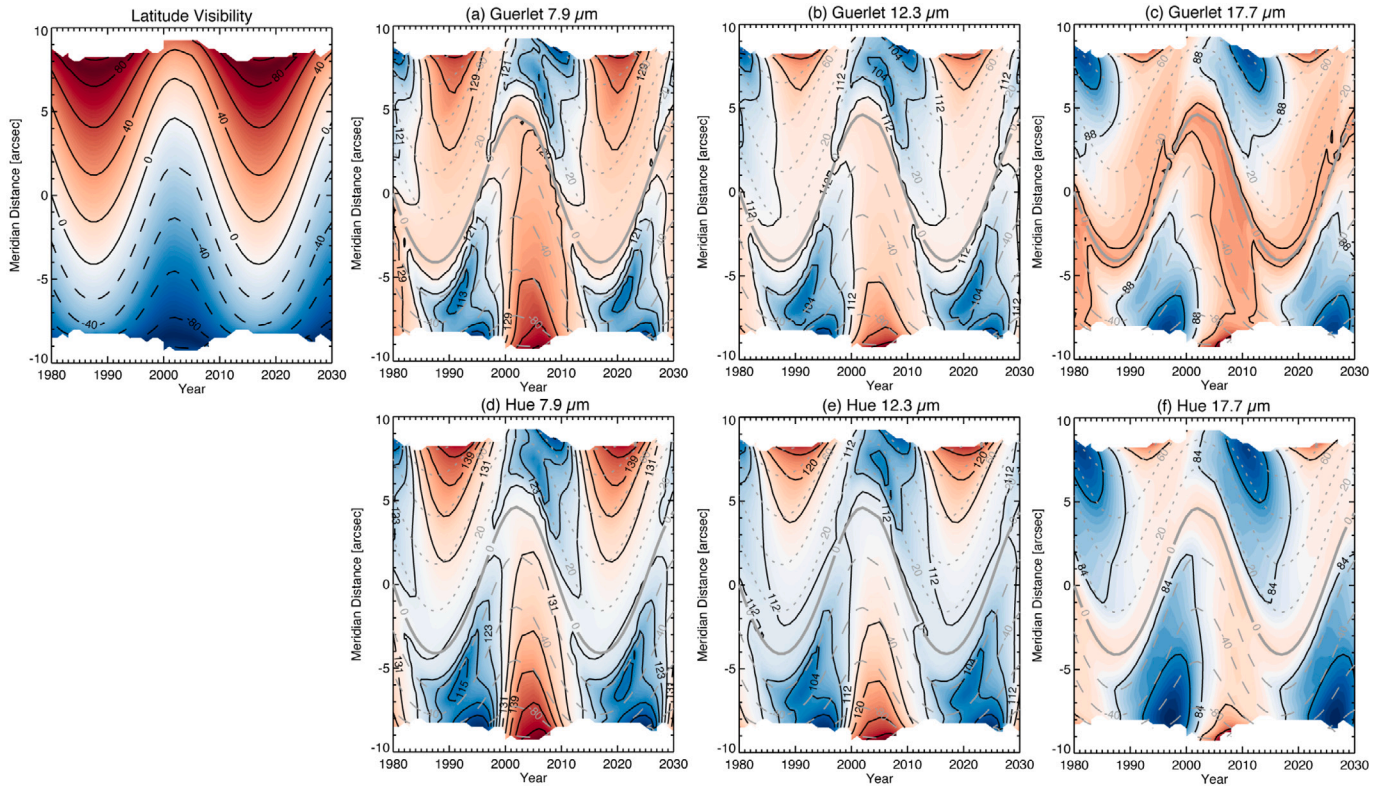


Fig. 14. Model-based synthetic brightness temperatures (K) along Saturn's central meridian, calculated for opposition in each year from 1980 to 2030. Values for T_B are given by the solid black contours in panels (a)–(f). Three representative filters are shown (7.9, 12.3 and 17.6 μm), for the radiative models of Guerlet et al. (2014) (top row) and Hue et al. (2016) (bottom row). Brightnesses are estimated on a $0.25''$ grid, with the zero-point being the centre of Saturn's disc. Visible latitudes are shown in the top left (colours represent latitudes from blue in the south to red in the north), and the same latitudes are superimposed in grey on the brightness temperatures in 20° steps (solid grey for the equator, dotted grey for northern latitudes, dashed grey for southern latitudes). (For interpretation of the references to colour in this figure legend, the reader is referred to the web version of this article.)

observations in 2019 failed). Nevertheless, observations between 2017 and 2022 are available to test the evolution of the equatorial oscillation and the expectation from Fig. 14 that the NPSV would continue to brighten until around 2021–22. Brightness temperatures averaged within $\pm 30^\circ$ of the central meridian are shown in Fig. 15 at 7.9, 12.3 and 17.7 μm . These profiles were calibrated by scaling to Cassini/CIRS mid-latitude brightnesses in 2017 (from 15°N to 45°N), avoiding changes associated with the equatorial oscillation and polar vortices. Latitudinal variability observed in these zonal averages is an order of magnitude larger to the standard error on the zonal mean. We also computed synthetic VISIR and COMICS images for 2017 and 2020, respectively, but both based on 2017 temperatures and hydrocarbon distributions — these are shown as the dotted lines in Fig. 15, and reveal how mid-IR emission would change based solely on the small shift in viewing geometry over this time period, and the small change in plate scale between the COMICS and VISIR detectors. At our mid-latitude reference point of $15 - 45^\circ\text{N}$, Fig. 15 shows that we would expect brightness changes of 1 K, 2 K, 0.5 K at 7.8- μm , 12.2 μm and 17.6 μm (respectively), simply due to the change in geometry and instrument. Unfortunately, this change cannot be captured by scaling solely to 2017 Cassini/CIRS measurements, so only variations exceeding these values can be considered as robust.

At 7.9 μm (Fig. 15a), the brightness temperatures are remarkably consistent from 2017 to 2020, such that the 2020 COMICS observations can be largely reproduced with the 2017 CIRS measurements. The final measurements in 2021 and 2022 then show a rather sudden shift in temperature, with the pole being ~ 5 K warmer than the 2017–2020 observations. The 2021 and 2022 VISIR observations both featured imaging on two nights, and the enhanced equator-to-pole gradient was seen in all four images, so is not an artefact of terrestrial observing conditions, nor were any background flux gradients identified across

the detector. The greater contrast between the NPSV and mid-latitudes can also be seen qualitatively in the 7.9 μm images in Fig. 2. Following the predictions of Guerlet et al. (2014) and Hue et al. (2016) in Fig. 14, these 2021–22 observations should be capturing the NPSV at its brightest, with a decline expected in subsequent years. The 2021–22 brightness scans show a stronger equator-to-pole gradient than all images examined thus far.

At 12.2 μm (Fig. 15b), almost all of the observed brightness change (2–3 K) falls within the expected range based on a geometry shift alone. The basic appearance of the 12.2- μm banded structure remains unchanged, but we see that both the 2020 COMICS and 2021–22 VISIR observations show a stronger equator-to-pole gradient than the 2017–18 data, again consistent with ongoing warming of the NPSV predicted by the radiative and photochemical models in Fig. 14.

At low latitudes, the 2017 and 2018 7.9- μm data confirm a low-latitude temperature minimum, but the 2020–2022 observations reveal the redevelopment of the temperature maximum last seen in 2013. This warm band still looks nothing like the strong temperature maximum observed at the last northern summer solstice (Gezari et al., 1989; Orton et al., 2008). Ethane emission at 12.4 μm shows a clearer local maximum at the equator in all years, indicating that the 7.9 and 12.4 μm filters sound different altitude regions of the vertical wave pattern.

Finally, the belt/zone contrasts visible at 17.7 μm (Fig. 15c) are very similar from 2017 to 2022, such that the connection between temperatures and winds (Section 3.2) holds throughout this time period. Only small changes are expected at 17.7 μm based on the changing geometry, but the latitudinal changes at the $\sim 1\text{-K}$ level are likely due to variable observing conditions between the four observing runs. Nevertheless, the north polar cyclone (NPC) appears to be at its brightest in 2022 (~ 97 K) than at any previous point in this time series, and the surrounding polar troposphere (poleward of approximately 50°N) appears

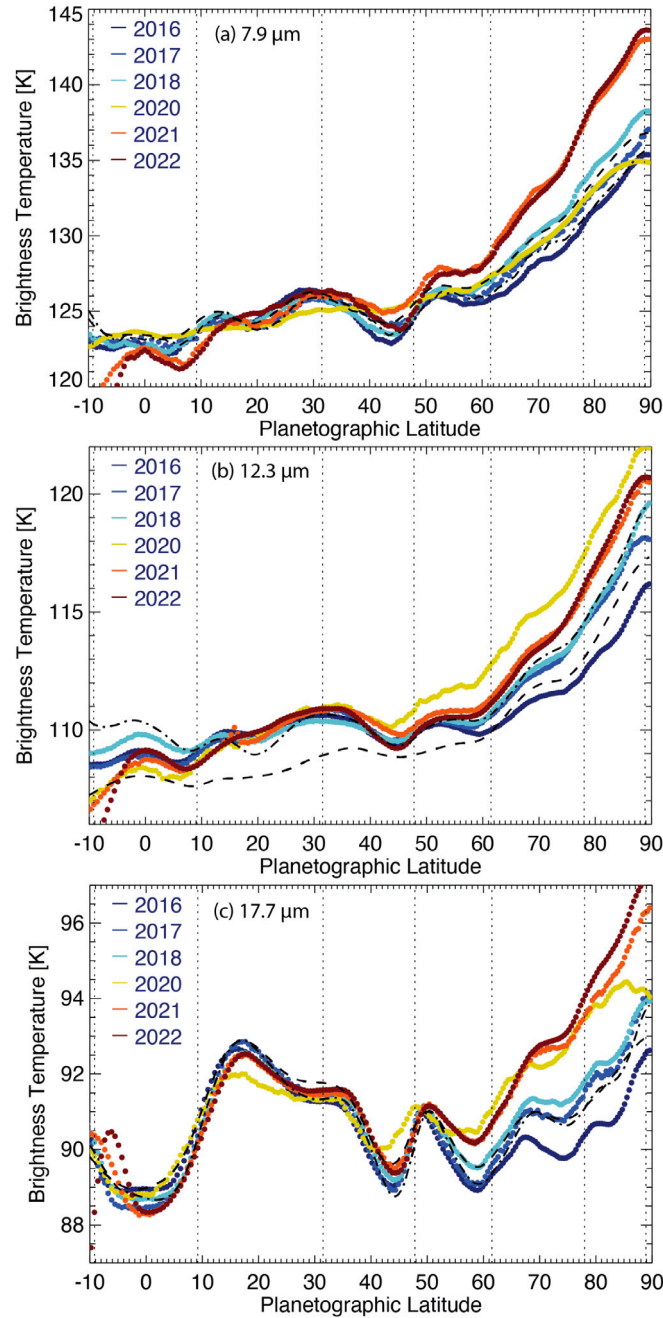


Fig. 15. Saturn brightness temperatures in three filters for the years following the end of the Cassini mission. Data are shown from VISIR in 2016, 2017, 2018, 2021, and 2022, showing a clear trend of warming poleward of 45°N. Observations from COMICS in July 2020 are added, to plug a gap in the time series, but we note that COMICS used slightly different filters and a coarser platescale, making it hard to compare quantitatively to VISIR. All have been calibrated to match CIRS brightnesses between 15–45°N in 2017. Synthetic brightness temperatures, based on those measured in 2017 by Cassini, are shown for 2017 VISIR (dot-dashed line) and 2020 COMICS (dashed line) to indicate the expected range of the observations if the temperatures are unchanging since 2017. The location of local maxima (eastward) jets in the Cassini-derived wind field (García-Melendo et al., 2011) are marked with vertical dotted lines.

to have warmed by 3–4 K since 2016, likely in response to continued seasonal warming of the NPSV.

For both the low-latitude oscillations, and the evolution of the NPSV at high latitudes, the changes from 2017 to 2022 are often rather subtle. Trends like the reestablishment of the local equatorial maximum, and the predicted cooling of the NPSV after 2022, will become clearer as the time series is extended into the 2020s.

6. Conclusion

Ground-based observatories have been monitoring Saturn's mid-infrared emission for almost four decades (1984–2022), spanning more

than a full Saturnian year ($L_s = 50^\circ$ to $L_s = 140^\circ$) and providing seasonal context for observations by the Cassini spacecraft (2004–2017, $L_s = 293 - 93^\circ$). This study used filtered images between 7 and 25 μm to tackle three themes: (i) the ability of Cassini-derived temperature and composition to reproduce the seasonal asymmetries and belt/zone structure observed in high-resolution images from 8-m primary mirrors; (ii) the repeatability of Saturn's temperature asymmetries, equatorial oscillations, and warm polar vortices from one Saturn year to the next; and (iii) the continued evolution of Saturn's northern summertime temperatures in the five years since the demise of Cassini. The quality of infrared imaging has improved tremendously

during the time span considered here, from the raster-scanned images from the 3-m IRTF (1984–1991), to 2D cameras (including MIRAC2 1993–1996 and MIRLIN 1996–2004), to the VLT/VISIR (2008–2022) and Subaru/COMICS (2005–2020) instruments on 8-m-class facilities. This change in observational quality, combined with the difficulty of consistent radiometric calibrations, makes quantitative assessments of atmospheric variability rather challenging. Nevertheless, this long-term survey allows us to draw the following conclusions:

1. **Seasonal Contrasts:** Synthetic images generated using Cassini-derived temperatures and composition successfully reproduce seasonal trends and the banded structure observed in thermal images from VLT/VISIR and Subaru/COMICS, including seasonal brightness temperature changes of ~ 30 K in the stratosphere and $\sim 10 - 15$ K in the troposphere from solstice to solstice. The latitudes and contrasts associated with Saturn's banded thermal structure are reproduced very well, as are the timescales for the growth and dissipation of emission from the polar stratospheric vortices (NPSV and SPSV) and compact polar cyclones (NPC and SPC) that were observed between 2004 and 2017. The brightest north polar emission during the mission was observed in 2017, consistent with the continued warming of the NPSV at northern summer solstice ($L_s = 90^\circ$, May 2017). In most cases, this validates the Cassini record of temperatures and hydrocarbons, but we note that images near $10.7 \mu\text{m}$ (sensitive to PH_3) were not well reproduced, suggesting that latitudinal and temporal variability of PH_3 must be taken into account in future studies. By stacking the filtered images to form a crude spectrum, we are able to estimate the vertical temperature structure as a function of latitude for the Earth-facing hemisphere, reproducing that observed by Cassini to within ~ 5 K.
2. **Belt/zone structure:** VISIR and COMICS images reveal the banded structure of Saturn's atmosphere, displaying 4–5 warm zonally-symmetric bands in each hemisphere. These bands are present in filters sensing all altitudes from ~ 500 mbar to the ~ 1 -mbar level. Converting the latitudinal brightness temperature gradients into a 'pseudo-shear' analogous to vertical windshear, we find a good negative correlation between the zonal wind speed and the strength of the shear. This implies that westward jets experience eastward (positive) shear, and eastward jets experience westward (negative) shear throughout the troposphere and stratosphere, consistent with the decay of the zonal winds with altitude. This strong connection between the winds and the banded thermal structure provides a better definition of Saturn's belts and zones than the muted albedo contrasts observed in visible light, and the fine-scale structure observed at $5 \mu\text{m}$ (Fletcher et al., 2011a). This banded structure is suggestive of Ferrel-like circulation cells on the scale of Saturn's zonal jets, with rising motions in cool zones, and subsidence in warmer belts. The same pattern is observed in Jupiter's upper troposphere (Fletcher et al., 2020). Thermal images from VLT and Subaru can monitor the banded contrasts (and windshear) associated with these circulation cells, and even reveal the hexagonal structure of the warm band near to the north pole. The thermal hexagon is observed at the edge of the NPSV in both troposphere- and stratosphere-sensing filters, confirming that the hexagon extends hundreds of kilometres above the visible clouds.
3. **Interannual Variability:** Observations from the IRTF allow us to study the thermal structure of Saturn over a full Saturnian year, and to compare to the predictions of radiative-climate and radiative-photochemical models. Although systematic differences between observations and models persist, the models successfully reproduce the timing of polar enhancements in temperatures in each year, lagging behind the solstices by a phase

difference that increases with pressure. This good correspondence suggests that Saturn's thermal field is largely repeatable from year to year. The first occurrence of the NPSV in 1984–1985 and 2014, and SPSV in 2000, are consistent with both models, confirming that this is primarily a radiative heating effect, albeit with a sharp boundary to the polar vortices introduced by dynamics. Furthermore, the tropospheric polar warming observed at $17\text{--}20 \mu\text{m}$ is also successfully reproduced by the models. However, the temporal sampling of our existing dataset is insufficient to distinguish the subtle differences between models that hold hydrocarbons fixed (Guerlet et al., 2014) and those that allow them to vary due to photochemistry (Hue et al., 2016). The only sources of interannual variability, therefore, are dynamic phenomena that are not tied to Saturn's seasons, such as storm eruptions (Fletcher et al., 2012) or the equatorial oscillation (see below).

4. **Equatorial Oscillation:** Mid-IR images acquired one Saturnian year apart, by VISIR in 2018 and the observations of Gezari et al. (1989) in 1989, reveal changes in the equatorial stratospheric $7.9\text{-}\mu\text{m}$ emission that are not consistent with a ~ 15 -year 'semi-annual' period of Saturn's Equatorial Stratospheric Oscillation (Orton et al., 2008). The warm equatorial band observed in 1989 was not present in 2018, although data in 2020–22 reveal the reemergence of the warm band. A similar inter-annual variation between Voyager and Cassini observations one year apart had been noted previously (Sinclair et al., 2014; Fletcher et al., 2016). Qualitative inspection of the imaging data suggests either (i) a longer ~ 20 -year period for the $7.9\text{-}\mu\text{m}$ oscillation; or (ii) interruptions to the progression of the equatorial oscillation by tropospheric meteorology, leading to natural variability from year to year. Intriguingly, infrared images in 1990 showed strong thermal perturbations in the equatorial stratosphere, possibly associated with the 1990 equatorial storm (Sánchez-Lavega et al., 1991) in the same way as was observed in 2011 (Fletcher et al., 2012). Continued observations in the 2020s will be needed to re-establish the period and phase of the equatorial stratospheric oscillation.
5. **Beyond Cassini:** Mid-infrared images from 2017–2022 have been used to extend the legacy of the Cassini observations, confirming continued atmospheric evolution through northern summer, approaching autumn equinox in May 2025 ($L_s = 180^\circ$). In particular, the NPSV continued to warm by approximately ~ 5 K at the $0.5\text{--}5.0$ mbar level, and $3\text{--}4$ K at the $100\text{--}200$ mbar level, by August 2022 ($L_s = 148^\circ$), and the warm equatorial stratospheric band re-emerged in ~ 2020 for the first time since 2013. Radiative models predict that the NPSV should now begin to cool as it recedes from view, with the SPSV becoming visible again in the early 2030s.

The long-term time series of infrared emission provides a valuable test of both the Cassini record of Saturn's temperatures, and the radiative climate models developed using different assumptions about photochemistry and dynamics. Observations from 8-m-class facilities also reveal Saturn's banded circulation patterns and polar vortices in excellent detail, allowing us to monitor dynamic phenomena on the Earth-facing hemisphere. However, ambiguous conclusions arise even when we have four decades of observations, as short-term dynamics can perturb the expected long-term seasonal and equatorial oscillations. Short annual imaging runs offer an efficient means to continue to track Saturn's thermal variability, but additional progress could be made with high-resolution spectroscopy from the ground (e.g., from TEXES, Lacy et al., 2002) or space (e.g., JWST), providing stronger constraints on Saturn's vertical temperature structure and composition.

Table A.1

Mid-IR imaging data used in this study. Where dates are given with a range, the best observations from a multi-day observing run were selected.

Date	Telescope	Instrument	Prog. ID
1984-05-01/05	IRTF	Graber Rasters	–
1984-06-05/07	IRTF	Graber Rasters	–
1985-05-18/21	IRTF	Graber Rasters	–
1986-06-17/18	IRTF	Graber Rasters	–
1987-06-07	IRTF	Graber Rasters	–
1988-09-25	IRTF	Graber Rasters	–
1989-04-23	IRTF	Graber Rasters	–
1989-06-09	IRTF	Graber Rasters	–
1989-08-28/29	IRTF	Graber Rasters	–
1990-06-15	IRTF	Graber Rasters	–
1990-08-24/27	IRTF	Graber Rasters	–
1989-03-28	IRTF	Gezari Camera	–
1990-12-02/04	IRTF	Gezari Camera	–
1993-08-11/12	IRTF	MIRAC2	–
1995-11-05	IRTF	MIRAC2	–
1997-09-19/20	IRTF	MIRAC2	–
1995-06-19	Palomar	SPECTROCAM-10	–
1996-06-29	Palomar	SPECTROCAM-10	–
1995-07-06	IRTF	MIRLIN	–
1999-08-12	IRTF	MIRLIN	–
2000-12-30	IRTF	MIRLIN	–
2002-02-07	IRTF	MIRLIN	–
2003-02-25	IRTF	MIRLIN	–
2005-04-30	Subaru	COMICS	o05108
2007-12-12	Subaru	COMICS	o07173
2008-01-23	Subaru	COMICS	o07173
2009-01-13/14	Subaru	COMICS	o08153
2013-05-01	Subaru	COMICS	o13137
2017-05-17	Subaru	COMICS	o17408
2017-09-06/07	Subaru	COMICS	o17239
2018-05-25/26	Subaru	COMICS	o18126
2018-08-20/21	Subaru	COMICS	o18219
2019-05-26/27	Subaru	COMICS	o19201
2020-06-03	Subaru	COMICS	o20205
2020-07-31	Subaru	COMICS	o20111
2008-04-12/15	VLT	VISIR	381.C-0560
2008-05-17/22	VLT	VISIR	381.C-0560
2008-06-10	VLT	VISIR	381.C-0560
2009-04-20/24	VLT	VISIR	383.C-0164
2009-06-01/22/30	VLT	VISIR	383.C-0164
2009-12-24	VLT	VISIR	383.C-0164
2010-03-18/21	VLT	VISIR	084.C-0193
2010-04-01/23	VLT	VISIR	084.C-0193
2011-01-19/27/31	VLT	VISIR	386.C-0096
2011-02-08	VLT	VISIR	386.C-0096
2011-03-25/26	VLT	VISIR	386.C-0096
2011-05-25	VLT	VISIR	386.C-0096
2011-06-26	VLT	VISIR	287.C-5032
2011-07-20/24	VLT	VISIR	287.C-5032
2015-05-21	VLT	VISIR	095.C-0142
2015-08-27	VLT	VISIR	095.C-0142
2016-06-08	VLT	VISIR	097.C-0226
2016-07-29	VLT	VISIR	097.C-0226
2017-09-07/18	VLT	VISIR	099.C-0614
2018-05-29/30	VLT	VISIR	0101.C-0047
2018-07-16/28	VLT	VISIR	0101.C-0047
2021-11-01/03	VLT	VISIR	108.22B
2022-07-04	VLT	VISIR	109.2360
2022-08-14	VLT	VISIR	109.2360

Data availability

COMICS, VISIR and CIRS data are already available via archives; earlier data (pre-2003) are available on request as they have not yet been formally archived.

Acknowledgements

Blake, Fletcher, Melin, Roman, Bardet and Antuñano were supported by a European Research Council Consolidator Grant (under the

European Union's Horizon 2020 research and innovation programme, grant agreement No 723890) at the University of Leicester. Some of this research was carried out at the Jet Propulsion Laboratory, California Institute of Technology, under a contract with the National Aeronautics and Space Administration (80NM0018D0004). This research used the ALICE High Performance Computing Facility at the University of Leicester. We wish to thank the many observers and telescope operators who work long nights to provide the community with the data needed to advance planetary science, including (but not limited to) Dan Gezari, Thierry Fouchet, and Padma Yanamandra-Fisher. We thank Sandrine Guerlet and Vincent Hue for making their radiative model predictions available to the community. We thank student interns Charlotte Mason and Zheyu Li (Oxford University), supported by Caltech's Summer Undergraduate Research Fellowship program at JPL; and Shana Mastoon (Pasadena City College) supported by JPL's Student Independent Research Internship program. Maël Es-Sayeh was supported by the Observatoire de Paris for an internship at Leicester. Each of these students contributed to preliminary reductions of the datasets presented in this paper. Finally, we thank three anonymous reviewers for their careful assessment of this manuscript.

The NEMESIS radiative transfer and spectral retrieval tool (Irwin et al., 2008) is available via <https://github.com/nemesiscode/radtrancode>. The Cassini/CIRS seasonal record of retrieved temperature and hydrocarbons is available here: <https://github.com/leighfletcher/CassiniCIRS>.

This study was based on observations collected at the European Organisation for Astronomical Research in the Southern Hemisphere; on data collected at the Subaru Telescope, which is operated by the National Astronomical Observatory of Japan; and on data collected from the Infrared Telescope Facility, which is operated by the University of Hawaii under contract 80HQTR19D0030 with the National Aeronautics and Space Administration. Programme numbers are listed, where available, in Table A.1. The authors wish to recognize and acknowledge the very significant cultural role and reverence that the summit of Maunakea has always had within the indigenous Hawaiian community. We are most fortunate to have the opportunity to conduct observations from this mountain.

Appendix A. Data

See Table A.1.

References

- Acton, C.H., 1996. Ancillary data services of NASA's navigation and ancillary information facility. *Planet. Space Sci.* 44, 65–70.
- Annex, A., Pearson, B., Seignovet, B., Carcich, B., Eichhorn, H., Mapel, J., von Forstner, J., McAuliffe, J., del Rio, J., Berry, K., Aye, K.M., Steffo, M., de Val-Borro, M., Kulamani, S., Murakami, S.-y., 2020. SpicePy: a pythonic wrapper for the SPICE toolkit. *J. Open Sour. Softw.* 5 (46), 2050.
- Antuñano, A., Cosentino, R.G., Fletcher, L.N., Simon, A.A., Greathouse, T.K., Orton, G.S., 2021. Fluctuations in Jupiter's equatorial stratospheric oscillation. *Nat. Astron.* 5, 71–77.
- Bardet, D., Spiga, A., Guerlet, S., 2022. Joint evolution of equatorial oscillation and interhemispheric circulation in Saturn's stratosphere. *Nat. Astron.* 6, 804–811.
- Conrath, B.J., Gierasch, P.J., Leroy, S.S., 1990. Temperature and circulation in the stratosphere of the outer planets. *Icarus* 83, 255–281.
- Del Genio, A.D., Achterberg, R.K., Baines, K.H., Flasar, F.M., Read, P.L., Sánchez-Lavega, A., Showman, A.P., 2009. Saturn atmospheric structure and dynamics. In: Dougherty, M.K., Esposito, L.W., Krimigis, S.M. (Eds.), *Saturn from Cassini-Huygens*. Springer, pp. 113–159, (Ch. 6).
- Deutsch, L.K., Hora, J.L., Adams, J.D., Kassis, M., 2003. MIRS: a mid-Infrared spectrometer and imager. In: Iye, M., Moorwood, A.F.M. (Eds.), *Instrument Design and Performance for Optical/Infrared Ground-Based Telescopes*. In: *Proceedings of the SPIE*, vol. 4841, pp. 106–116.
- Duer, K., Gavriel, N., Galanti, E., Kaspi, Y., Fletcher, L.N., Oyafuso, F.A., Grassi, D., Ingersoll, A.P., Guillot, T., Bolton, S., 2021. Evidence for multiple ferrel cells on jupiter. *Geophys. Res. Lett.* 48 (23), e95651, <https://ui.adsabs.harvard.edu/abs/2021GeoRL.4895651D/abstract>.

- Flasar, F.M., Achterberg, R.K., Conrath, B.J., Pearl, J.C., Bjoraker, G.L., Jennings, D.E., Romani, P.N., Simon-Miller, A.A., Kunde, V.G., Nixon, C.A., Bézard, B., Orton, G.S., Spilker, L.J., Spencer, J.R., Irwin, P.G.J., Teanby, N.A., Owen, T.C., Brasunas, J., Segura, M.E., Carlson, R.C., Mamoutkine, A., Gierasch, P.J., Schinder, P.J., Showalter, M.R., Ferrari, C., Barucci, A., Courtin, R., Coustenis, A., Fouchet, T., Gautier, D., Lellouch, E., Marten, A., Prangé, R., Strobel, D.F., Calcutt, S.B., Read, P.L., Taylor, F.W., Bowles, N., Samuelson, R.E., Abbas, M.M., Raulin, F., Ade, P., Edgington, S., Pilorz, S., Wallis, B., Wishnow, E.H., 2005. Temperatures, winds, and composition in the saturnian system. *Science* 307, 1247–1251.
- Flasar, F.M., Kunde, V.G., Abbas, M.M., Achterberg, R.K., Ade, P., Barucci, A., Bézard, B., Bjoraker, G.L., Brasunas, J.C., Calcutt, S., Carlson, R., Césarsky, C.J., Conrath, B.J., Coradini, A., Courtin, R., Coustenis, A., Edberg, S., Edgington, S., Ferrari, C., Fouchet, T., Gautier, D., Gierasch, P.J., Grossman, K., Irwin, P., Jennings, D.E., Lellouch, E., Mamoutkine, A.A., Marten, A., Meyer, J.P., Nixon, C.A., Orton, G.S., Owen, T.C., Pearl, J.C., Prangé, R., Raulin, F., Read, P.L., Romani, P.N., Samuelson, R.E., Segura, M.E., Showalter, M.R., Simon-Miller, A.A., Smith, M.D., Spencer, J.R., Spilker, L.J., Taylor, F.W., 2004. Exploring the saturn system in the thermal infrared: the composite infrared spectrometer. *Space Sci. Rev.* 115, 169–297.
- Fletcher, L.N., Baines, K.H., Momary, T.W., Showman, A.P., Irwin, P.G.J., Orton, G.S., Roos-Serote, M., Merlet, C., 2011a. Saturn's tropospheric composition and clouds from Cassini/VIMS 4.6–5.1 μm nightside spectroscopy. *Icarus* 214, 510–533.
- Fletcher, L.N., Greathouse, T.K., Moses, J.I., Guerlet, S., West, R.A., 2018a. In: Baines, K.H., Flasar, F.M., Krupp, N., Stallard, T.S. (Eds.), *Saturn's Seasonally Changing Atmosphere: Thermal Structure, Composition and Aerosols*. Cambridge Planetary Science. Cambridge Univ. Press, New York (Ch. 10).
- Fletcher, L.N., Guerlet, S., Orton, G.S., Cosentino, R.G., Fouchet, T., Irwin, P.G.J., Li, L., Flasar, F.M., Gorius, N., Morales-Juberías, R., 2017. Disruption of Saturn's quasi-periodic equatorial oscillation by the Great Northern Storm. *Nat. Astron.* 1, 765–770.
- Fletcher, L.N., Hesman, B.E., Achterberg, R.K., Irwin, P.G.J., Bjoraker, G., Gorius, N., Hurley, J., Sinclair, J., Orton, G.S., Legarreta, J., García-Melendo, E., Sánchez-Lavega, A., Read, P.L., Simon-Miller, A.A., Flasar, F.M., 2012. The origin and evolution of Saturn's 2011–2012 stratospheric vortex. *Icarus* 221, 560–586.
- Fletcher, L.N., Hesman, B.E., Irwin, P.G.J., Baines, K.H., Momary, T.W., Sánchez-Lavega, A., Flasar, F.M., Read, P.L., Orton, G.S., Simon-Miller, A., Hueso, R., Bjoraker, G.L., Mamoutkine, A., del Río-Gaztelurrutia, T., Gomez, J.M., Buratti, B., Clark, R.N., Nicholson, P.D., Sotin, C., 2011b. Thermal structure and dynamics of saturn's northern springtime disturbance. *Science* 332, 1413–1417.
- Fletcher, L.N., Irwin, P.G.J., Achterberg, R.K., Orton, G.S., Flasar, F.M., 2016. Seasonal variability of Saturn's tropospheric temperatures, winds and para- H_2 from Cassini far-IR spectroscopy. *Icarus* 264, 137–159.
- Fletcher, L.N., Irwin, P.G.J., Teanby, N.A., Orton, G.S., Parrish, P.D., Calcutt, S.B., de Kok, R., Howett, C., Bowles, N., Taylor, F.W., 2007. Characterising saturn's vertical temperature structure from cassini/CIRS. *Icarus* 189, 457–478.
- Fletcher, L.N., Kaspi, Y., Guillot, T., Showman, A.P., 2020. How well do we understand the belt/zone circulation of giant planet atmospheres? *Space Sci. Rev.* 216 (2), 30.
- Fletcher, L.N., Orton, G.S., Sinclair, J.A., Guerlet, S., Read, P.L., Antuñaño, A., Achterberg, R.K., Flasar, F.M., Irwin, P.G.J., Bjoraker, G.L., Hurley, J., Hesman, B.E., Segura, M., Gorius, N., Mamoutkine, A., Calcutt, S.B., 2018b. A hexagon in Saturn's northern stratosphere surrounding the emerging summertime polar vortex. *Nature Commun.* 9, 3564.
- Fletcher, L.N., Orton, G.S., Teanby, N.A., Irwin, P.G.J., 2009a. Phosphine on jupiter and saturn from cassini/CIRS. *Icarus* 202, 543–564.
- Fletcher, L.N., Orton, G.S., Yanamandra-Fisher, P., Fisher, B.M., Parrish, P.D., Irwin, P.G.J., 2009b. Retrievals of atmospheric variables on the gas giants from ground-based mid-infrared imaging. *Icarus* 200, 154–175.
- Fletcher, L.N., Oyafuso, F.A., Allison, M., Ingersoll, A., Li, L., Kaspi, Y., Galanti, E., Wong, M.H., Orton, G.S., Duer, K., Zhang, Z., Li, C., Guillot, T., Levin, S.M., Bolton, S., 2021. Jupiter's temperate belt/zone contrasts revealed at depth by juno microwave observations. *J. Geophys. Res. (Planets)* 126 (10), e06858.
- Fouchet, T., Guerlet, S., Strobel, D., Simon-Miller, A., Bézard, B., Flasar, F., 2008. An equatorial oscillation in Saturn's middle atmosphere. *Nature* 453 (7192), 200–202.
- Friedson, A.J., Moses, J.I., 2012. General circulation and transport in Saturn's upper troposphere and stratosphere. *Icarus* 218, 861–875.
- García-Melendo, E., Pérez-Hoyos, S., Sánchez-Lavega, A., Hueso, R., 2011. Saturn's zonal wind profile in 2004–2009 from Cassini ISS images and its long-term variability. *Icarus* 215, 62–74.
- Gezari, D.Y., Mumma, M.J., Espenak, F., Deming, D., Bjoraker, G., Woods, L., Folz, W., 1989. New features in Saturn's atmosphere revealed by high-resolution thermal infrared images. *Nature* 342, 777–780.
- Giles, R.S., Greathouse, T.K., Cosentino, R.G., Orton, G.S., Lacy, J.H., 2020. Vertically-resolved observations of Jupiter's quasi-quadrennial oscillation from 2012 to 2019. *Icarus* 350, 113905.
- Gillett, F.C., Orton, G.S., 1975. Center-to-limb observations of Saturn in the thermal infrared. *Astrophys. J.* 195, L47–L49.
- Glasse, A.C., Atad-Ettinger, E.I., Harris, J.W., 1997. *Michelle Midinfrared Spectrometer and Imager*. In: Ardeberg, A.L. (Ed.), *Society of Photo-Optical Instrumentation Engineers (SPIE) Conference Series*. Vol. 2871, pp. 1197–1203.
- Greathouse, T.K., Lacy, J.H., Bézard, B., Moses, J.I., Griffith, C.A., Richter, M.J., 2005. Meridional variations of temperature, C_2H_2 and C_2H_4 abundances in Saturn's stratosphere at southern summer solstice. *Icarus* 177, 18–31.
- Guerlet, S., Fouchet, T., Bézard, B., Simon-Miller, A.A., Flasar, F.M., 2009. Vertical and meridional distribution of ethane, acetylene and propane in Saturn's stratosphere from CIRS/Cassini limb observations. *Icarus* 203, 214–232.
- Guerlet, S., Spiga, A., Sylvestre, M., Indurain, M., Fouchet, T., Leconte, J., Millour, E., Wordsworth, R., Capderou, M., Bézard, B., Forget, F., 2014. Global climate modeling of Saturn's atmosphere. Part I: Evaluation of the radiative transfer model. *Icarus* 238, 110–124.
- Hanel, R., Conrath, B., Flasar, F.M., Kunde, V., Maguire, W., Pearl, J.C., Pirraglia, J., Samuelson, R., Cruikshank, D.P., Gautier, D., Gierasch, P.J., Horn, L., Ponnampereuma, C., 1982. Infrared observations of the Saturnian system from Voyager 2. *Science* 215, 544–548.
- Hanel, R., Conrath, B., Flasar, F.M., Kunde, V., Maguire, W., Pearl, J.C., Pirraglia, J., Samuelson, R., Herath, L., Allison, M., Cruikshank, D.P., Gautier, D., Gierasch, P.J., Horn, L., Koppany, R., Ponnampereuma, C., 1981. Infrared observations of the Saturnian system from Voyager 1. *Science* 212, 192–200.
- Hoffmann, W.F., Fazio, G.G., Shivanandan, K., Hora, J.L., Deutsch, L.K., 1993. MIRAC: a mid-infrared array camera for astronomy. In: Fowler, A.M. (Ed.), *Infrared Detectors and Instrumentation*. In: *Society of Photo-Optical Instrumentation Engineers (SPIE) Conference Series*, vol. 1946, pp. 449–460.
- Holton, J., 2004. *An Introduction to Dynamic Meteorology*. Academic Press.
- Hue, V., Greathouse, T.K., Cavalié, T., Dobrijevic, M., Hersant, F., 2016. 2D photochemical modeling of Saturn's stratosphere. Part II: Feedback between composition and temperature. *Icarus* 267, 334–343.
- Irwin, P., Teanby, N., de Kok, R., Fletcher, L., Howett, C., Tsang, C., Wilson, C., Calcutt, S., Nixon, C., Parrish, P., 2008. The NEMESIS planetary atmosphere radiative transfer and retrieval tool. *J. Quant. Spectrosc. Radiat. Transfer* 109 (6), 1136–1150.
- Katata, H., Okamoto, Y.K., Yamashita, T., Miyata, T., Sako, S., Takubo, S., Honda, M., Onaka, T., Nakamura, K., 2002. COMICS: cooled mid-infrared camera and spectrometer for the subaru telescope. In: Ikeuchi, S., Hearnshaw, J., Hanawa, T. (Eds.), *8th Asian-Pacific Regional Meeting, Volume II*. pp. 17–18.
- Lacy, J.H., Richter, M.J., Greathouse, T.K., Jaffe, D.T., Zhu, Q., 2002. TEXES: a sensitive high-resolution grating spectrograph for the mid-infrared. *Publ. Astron. Soc. Pac.* 114, 153–168.
- Lagage, P.O., Pel, J.W., Authier, M., Belorgey, J., Claret, A., Doucet, C., Dubreuil, D., Durand, G., Elswijk, E., Girardot, P., Käufel, H.U., Kroes, G., Lortholary, M., Lussignol, Y., Marchesi, M., Pantin, E., Peletier, R., Pirard, J., Prag, J., Rio, Y., Schoenmaker, T., Siebenmorgen, R., Silber, A., Smette, A., Sterzik, M., Veyssiere, C., 2004. Successful commissioning of VISIR: the mid-infrared VLT instrument. *Messenger* 117, 12–16.
- Moses, J.I., Armstrong, E.S., Fletcher, L.N., Friedson, A.J., Irwin, P.G.J., Sinclair, J.A., Hesman, B.E., 2015. Evolution of stratospheric chemistry in the Saturn storm beacon region. *Icarus* 261, 149–168.
- Okamoto, Y.K., Katata, H., Yamashita, T., Miyata, T., Sako, S., Takubo, S., Honda, M., Onaka, T., 2003. Improved performances and capabilities of the cooled mid-infrared camera and spectrometer (COMICS) for the subaru telescope. In: Iye, M., Moorwood, A.F.M. (Eds.), *Instrument Design and Performance for Optical/Infrared Ground-Based Telescopes*. In: *Proceedings of the SPIE*, vol. 4841, pp. 169–180.
- Orton, G.S., Yanamandra-Fisher, P.A., 2005. Saturn's temperature field from high-resolution middle-infrared imaging. *Science* 307, 696–698.
- Orton, G., Yanamandra-Fisher, P., Fisher, B., Friedson, A., Parrish, P., Nelson, J., Bauermeister, A., Fletcher, L., Gezari, D., Varosi, F., Tokunaga, A., Caldwell, J., Baines, K., Hora, J., Ressler, M., Fujiyoshi, T., Fuse, T., Hagopian, H., Martin, T., Bergstralh, J., Howett, C., Hoffmann, W., Deutsch, L., Van Cleve, J., Noe, E., Adams, J., Kassiss, M., Tollestrup, E., 2008. Semi-annual oscillations in Saturn's low-latitude stratospheric temperatures. *Nature* 453, 196–198.
- Osprey, S.M., Butchart, N., Knight, J.R., Scaife, A.A., Hamilton, K., Anstey, J.A., Scheninger, V., Zhang, C., 2016. An unexpected disruption of the atmospheric quasi-biennial oscillation. *Science* 353, 1424–1427.
- Pirraglia, J.A., Conrath, B.J., Allison, M.D., Gierasch, P.J., 1981. Thermal structure and dynamics of saturn and jupiter. *Nature* 292 (5825), 677–679.
- Read, P.L., Conrath, B.J., Fletcher, L.N., Gierasch, P.J., Simon-Miller, A.A., Zuchowski, L.C., 2009. Mapping potential vorticity dynamics on saturn: Zonal mean circulation from Cassini and Voyager data. *Plan. Space Sci.* 57 (14–15), 1682–1698.
- Ressler, M., Werner, M., Cleve, J., Chou, H., 1994. The JPL deep-well mid-infrared array camera. *Exp. Astron.* 3 (1), 277–280.
- Sánchez-Lavega, A., Colas, F., Lecacheux, J., Laques, P., Parker, D., Miyazaki, I., 1991. The Great White SPOT and disturbances in Saturn's equatorial atmosphere during 1990. *Nature* 353, 397–401.
- Sinclair, J.A., Irwin, P.G.J., Fletcher, L.N., Greathouse, T., Guerlet, S., Hurley, J., Merlet, C., 2014. From Voyager-IRIS to Cassini-CIRS: Interannual variability in Saturn's stratosphere? *Icarus* 233, 281–292.
- Sinton, W.M., Macy, W.W., Good, J., Orton, G.S., 1980. Infrared scans of Saturn. *Icarus* 42 (2), 251–256.
- Vasavada, A.R., Hörst, S.M., Kennedy, M.R., Ingersoll, A.P., Porco, C.C., Del Genio, A.D., West, R.A., 2006. Cassini imaging of Saturn: Southern hemisphere winds and vortices. *J. Geophys. Res. (Planets)* 111 (E10), 5004.